Adrenergic activation modulates the signal from the Reissner fiber to cerebrospinal fluid-contacting neurons during development

Yasmine Cantaut-Belarif, Adeline Orts Del'Immagine, Margot Penru, Guillaume Pézeron, Claire Wyart, Pierre-Luc Bardet

Title

Adrenergic activation modulates the signal from the Reissner fiber to cerebrospinal fluid-contacting neurons during development

Authors

Cantaut-Belarif Yasmine[1], Orts-Del'Immagine Adeline[1], Penru Margot[1], Pézeron Guillaume[2], Wyart Claire[1]*, Bardet Pierre-Luc[1]*

Affiliations

1: Paris Brain Institute, ICM, Inserm U 1127, CNRS UMR 7225, Sorbonne Université, F-75013, Paris, France

2: Molecular Physiology and Adaptation (PhyMA - UMR 7221), Muséum National d'Histoire Naturelle, CNRS, Paris, France

*: co-corresponding authors

Abstract

The cerebrospinal fluid (CSF) contains an extracellular thread conserved in vertebrates, the Reissner fiber, which controls body axis morphogenesis in the zebrafish embryo. Yet, the signaling cascade originating from this fiber to ensure body axis straightening is not understood. Here, we explore the functional link between the Reissner fiber and undifferentiated spinal neurons contacting the CSF (CSF-cNs). First, we show that the Reissner fiber is required in vivo for the expression of urp2, a neuropeptide expressed in CSF-cNs. We show that the Reissner fiber is also required for embryonic calcium transients in these spinal neurons. Finally, we study how local adrenergic activation can substitute for the Reissner fiber-signaling pathway to CSF-cNs and rescue body axis morphogenesis. Our results show that the Reissner fiber acts on CSF-cNs and thereby contributes to establish body axis morphogenesis, and suggest it does so by controlling the availability of a chemical signal in the CSF.

Introduction

One of the major questions in the study of multicellular organism development is to understand how precise morphogenesis is ensured during embryonic and postembryonic stages while the animal grows into an adult. In particular, this process requires coordination between cell specification signals and the control of the tissue shape (Chan et al., 2017). It has recently emerged that the cerebrospinal fluid (CSF) contains many signals important for cell differentiation, and is an important route for the control of morphogenesis (Fame and Lehtinen, 2020). The CSF is a complex liquid filling the central nervous system cavities containing a set of diffusible signaling cues guiding neurogenesis (Lehtinen et al., 2011) and brain morphology in a tissue autonomous manner (Kaiser et al., 2019; Langford et al., 2020). The CSF circulation is in part generated by the coordinated movement of cilia projecting to the lumen of brain ventricles and central canal of the spinal cord (Faubel et al., 2016; Hagenlocher et al., 2013; Olstad et al., 2019; Sternberg et al., 2018; Thouvenin et al., 2020).

The role of cilia in the control of CSF composition and circulation has recently gained a special attention in zebrafish. Indeed, disruption of cilia motility in this species has been long known to induce a typical phenotype consisting in a downward curvature of the posterior axis of the embryo (Brand et al., 1996; Jaffe et al., 2016; Kramer-Zucker et al., 2005; Sullivan-Brown et al., 2008). This phenotype has recently been linked to a role of the CSF in body axis curvature establishment and maintenance downstream of cilia function (Cantaut-Belarif et al., 2018; Grimes et al., 2016). We previously showed that the Reissner fiber (RF), a component of the CSF, is important for axis morphogenesis in the zebrafish embryo(Cantaut-Belarif et al., 2018). The Reissner fiber (Reissner, 1860) is an acellular proteinous thread bathing in the brain and spinal cord cavities early in development (Troutwine et al., 2019), formed by the aggregation of the SCO-spondin glycoprotein, secreted into the CSF by the subcommissural organ and the floor plate (Lehmann and Naumann, 2005; Meiniel et al., 2008). This fiber fails to assemble in cilia-defective mutants, and *scospondin* mutant embryos lacking the Reissner fiber exhibit a curled-down axis despite exhibiting normal cilia motility and CSF flow (Cantaut-Belarif et al., 2018; Rose et al., 2020). These observations suggest that the fiber itself plays a role in the control of body axis morphogenesis in the embryo, and that its absence causes a curled-down phenotype, including in cilia-defective mutants. However, the signal linking the presence of the Reissner fiber and its long-range effect on body axis morphogenesis is not fully understood.

Recent studies suggest that bath applications of monoamines can restore a straight axis in embryos with a curled-down phenotype (Lu et al., 2020; Zhang et al., 2018). Monoamines are widespread neurotransmitters and neuromodulators that include

epinephrine and norepinephrine, and influence many neurophysiological processes in the adult such as sleep control (Singh et al., 2015). Radiolabeled norepinephrine can bind the Reissner fiber in the CSF of rats (Caprile et al., 2003) and frogs (Diederen et al., 1983). The study of their role in development is emerging, with a special focus on neuronal precursors proliferation and differentiation (Berg et al., 2013).

In addition, the signal controlling axis morphogenesis downstream of CSF flow has been associated with changes in the expression of Urp1 and Urp2 peptides (Lu et al., 2020; Zhang et al., 2018). These peptides belong to a family of neuropeptides similar to Urotensin-II previously shown to mediate endocrine, cardiac and neurophysiological functions (Vaudry et al., 2015). In the zebrafish embryo, *urp1* and *urp2* are expressed along the antero-posterior axis of the neural tube in a subset of spinal sensory neurons (Quan et al., 2015) called CSF-contacting neurons (CSF-cNs). CSF-cNs extend into the CSF a microvilliated apical extension that starts differentiating in the embryo and becomes fully mature in the larva to tune the mechanosensory responses of CSF-cNs upon tail bending (Desban et al., 2019). These conserved interoceptive neurons form two populations of different developmental origins that are located ventrally and dorso-laterally relative to the central canal of the zebrafish spinal cord (Djenoune et al., 2017; Park et al., 2004). At the embryonic stage, undifferentiated CSF-cNs that are located ventrally in the neural tube are the only ones expressing Urp neuropeptides and exhibiting spontaneous calcium transients at rest (Sternberg et al., 2018). Recently, the Reissner fiber was shown to be required in the larva for the mechanosensory function leading to intracellular calcium increase in differentiated CSF-cNs (Orts-Del'Immagine et al., 2020). However, the role of the Reissner fiber in CSF-cN spontaneous activity at the embryonic stage when they express Urp neuropeptides is unknown.

In this study, we aimed to better understand the signal linking the Reissner fiber to body axis morphogenesis. To investigate whether the Reissner fiber is required for a signal towards the immature CSF-cNs, we sought to decipher the nature of this signal and how it affects at long distance body axis straightening. We show that the Reissner fiber is required for a signal controlling *urp2* expression. Using *in vivo* calcium imaging, we report that the Reissner fiber is also required for calcium signaling in *urp2*-expressing ventral CSF-cNs, confirming the existence of a crosstalk between the Reissner fiber and undifferentiated CSF-cNs at the embryonic stage. Using the *pkd2l1* mutant, we show that the loss of calcium signaling in ventral CSF-cNs does not lead to a loss of *urp2* expression nor embryonic body axis curvature. Finally, we show that epinephrine and norepinephrine can restore the Reissner fiber-dependent signal when injected locally in the brain ventricles, and can restore body axis defects of *scospondin* mutants. Our work demonstrates that the Reissner fiber-

dependent signal to ventral CSF-cNs contributes to body axis straightening and is modulated by adrenergic ligands.

Results and Figures

The Reissner fiber controls *urp2* gene expression

To explore the signals downstream the Reissner fiber, we performed a transcriptomic analysis of *scospondin* mutants (Figure 1).

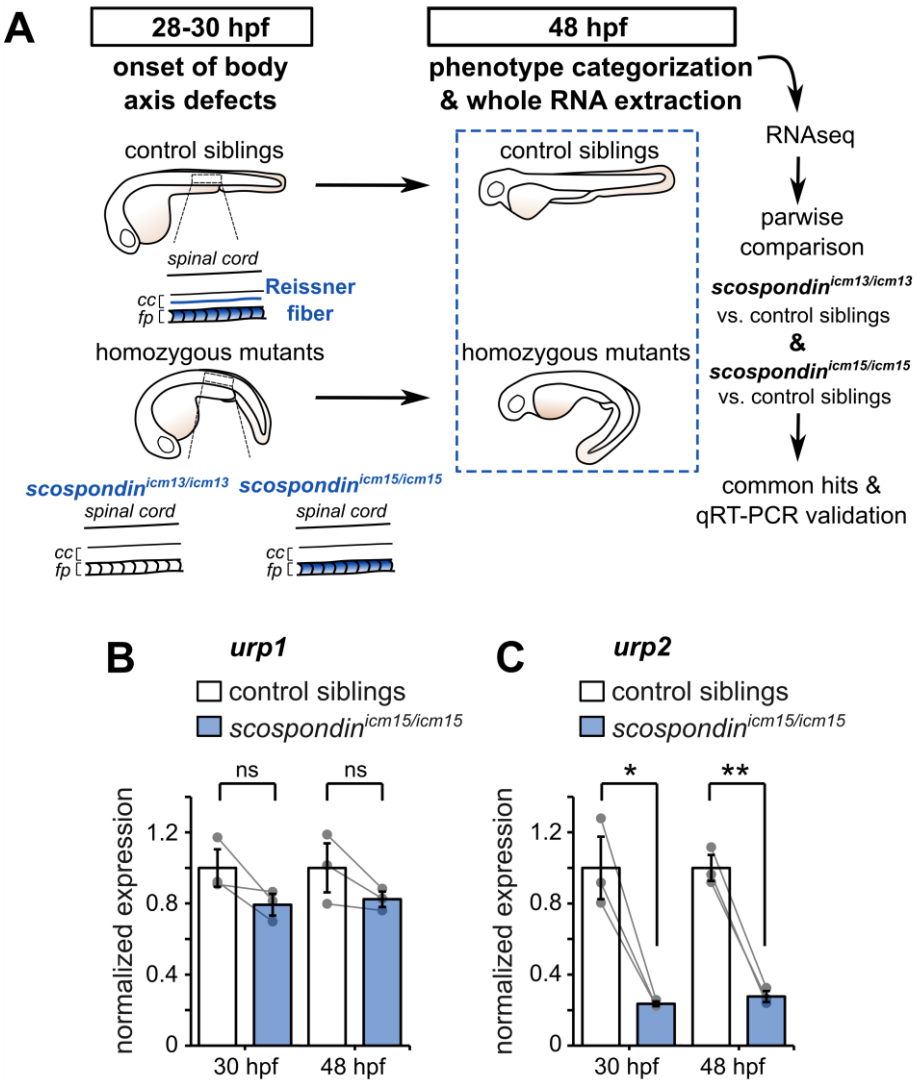

Figure 1. The Reissner fiber is required for *urp2* but not *urp1* gene expression.
(**A**) Schematic of the experimental design. Embryos obtained from *scospondin*$^{icm15/+}$ or *scospondin*$^{icm13/+}$ incrosses were raised until 48 hpf and categorized according to their external phenotype: straight body axis (control siblings, top) or curled-down body axis (homozygous mutants, bottom) prior to RNA extraction. RNA sequencing was performed on 3 independent replicates for each allele and allowed pairwise comparisons of transcriptomes to identify commonly regulated genes. qRT-PCR experiments were performed at 30 hpf to validate transcriptomic data at the onset of body axis defects induced by the loss of the Reissner fiber and at 48 hpf when the phenotype is fully developed (48 hpf). Null *scospondin*$^{icm13/icm13}$ and hypomorphic *scospondin*$^{icm15/icm15}$ mutant embryos share the same peculiar curled-down phenotype induced by the loss of the Reissner fiber in the

central canal of spinal cord (cc). However, *scospondin*$^{icm15/icm15}$ mutants retain SCO-spondin protein expression in secretory structures such as the floor plate (fp). (**B**, **C**) qRT-PCR analysis of mRNA levels of *urp1* (**B**) and *urp2* (**C**) in *scospondin*$^{icm15/icm15}$ mutants (blue) compared to their control siblings (white) at 30 and 48 hpf. Data are represented as mean ± SEM. N = 3 independent biological replicates for each condition. Each point represents a single experimental replicate. ns p>0.05, * p<0.05, ** p<0.01 (paired t-test).
See also Figure Supplement 1 and Source Data 1 & 2.

We took advantage of two previously-generated *scospondin* alleles (Cantaut-Belarif et al., 2018) to evaluate transcriptional modifications associated with the curled-down phenotype due to the loss of the Reissner fiber in the CSF. While the *scospondin*^{icm13} null allele leads to a dual loss of the fiber in the central canal and of the SCO-spondin protein detection in secretory structures, the *scospondin*^{icm15} hypomorphic allele retains protein expression but solely precludes the Reissner fiber formation (Figure 1A). Both homozygous mutants lack the Reissner fiber and exhibit a typical curled-down phenotype, which arises from 28-30 hours post-fertilization (hpf) onwards and was undetectable beforehand (Cantaut-Belarif et al., 2018), Figure 1A, Figure 1-figure supplement 1). We performed pairwise comparisons of the transcriptomes of homozygous mutants *versus* control siblings at 48 hpf when the body axis curvature defect is fully penetrant (Cantaut-Belarif et al., 2018). The resulting lists of up- and down-regulated transcripts that were common to the two *scospondin* alleles are presented in Figure 1-Source Data 2. Very few genes exhibited an important change in expression, and only a handful changed more than two folds. Noticeably, we observed a strong reduction of *urp2* gene expression in curled-down mutant embryos lacking the Reissner fiber compared to their control siblings (mean ± SEM fold decrease: 4.07 ± 1.2 in *scospondin*$^{icm13/icm13}$ and 4.69 ± 1.77 in *scospondin*$^{icm15/icm15}$, n=3 replicates each, p-value < 0.00005, GLM test; see Material and Methods and Figure 1-Source Data 2 for details). There was no significant decrease in *urp1* transcript levels (mean ± SEM fold decrease: 0.97 ± 0.06 in *scospondin*$^{icm13/icm13}$ and 1.22 ± 0.25 in *scospondin*$^{icm15/icm15}$, n=3 replicates each, p-value = p=0.191, GLM test).

The gene *urp2* encodes for a secreted neuropeptide belonging to the Urotensin-II-related-peptide family (Tostivint et al., 2014). Together with *urp1*, these transcripts have recently been identified as both strongly downregulated in curled-down mutants (Lu et al., 2020; Zhang et al., 2018). To ascertain our RNAseq results and confirm the difference we observed with previous results, we carried out qRT-PCR analysis of *urp1* and *urp2* expression levels in the hypomorphic *scospondin*^{icm15} allele. Interestingly, we observed that *urp1* expression level is not significantly decreased in *scospondin* homozygous mutants compared to their control siblings, neither at 30 hpf nor at 48 hpf (Figure 1B). Consistently

with transcriptomic results, *urp2* expression level shows a strong decrease at 48 hpf in mutant embryos compared to their control siblings (3.6 ± 0.2 fold decrease; mean ± SEM; Figure 1C). This is also true at the onset of the curled-down phenotype (30 hpf: 4.2 ± 0.5 fold decrease; mean ± SEM; Figure 1C) indicating that *urp2* gene expression level is affected when embryos start to develop an abnormal morphogenesis of the posterior axis. Taken together, these data show that in zebrafish embryo the presence of the Reissner fiber in the CSF is required for the normal expression level of *urp2,* but not *urp1*.

The Reissner fiber is required for calcium signaling in *urp2* expressing CSF-cNs

The expression of Urotensin-II-related peptides is restricted to the ventral population of CSF-cNs (Quan et al., 2015), known to exhibit spontaneous intracellular calcium variations around 30 hpf (Sternberg et al., 2018) when the curled-down phenotype becomes visible in *scospondin* mutants (Cantaut-Belarif 2018 and Figure 1-figure supplement 1). Curled-down cilia-defective embryos lack these early calcium transients (Sternberg et al., 2018) and do not form a proper Reissner fiber (Cantaut-Belarif et al., 2018). We therefore hypothesized that the Reissner fiber may functionally interact with ventral CSF-cNs that are expressing *urp2*.

To address this question, we performed *in vivo* population calcium imaging at 28-30 hpf using the *Tg(pkd2l1:GCaMP5G)* line labeling the dorso-lateral and ventral CSF-cNs in the spinal cord (Figure 2A, Figure 2-video 1). As previously described, we observed that ventral CSF-cNs exhibit spontaneous calcium transients in wild type embryos (*scospondin*$^{+/+}$, Figure 2B, Figure 2-video 1). Quantification of the integrated fluorescence variations over time showed that in heterozygous *scospondin*$^{icm15/+}$ embryos, which display a straight body axis and form a proper Reissner fiber (Cantaut-Belarif et al., 2018), ventral CSF-cNs retained the same level of activity than in wild type (Figure 2C). On the contrary, homozygous *scospondin*$^{icm15/icm15}$ embryos exhibited a 52.8% decrease of calcium activity compared to wild type (Figure 2C). A similar reduction of 39% occurred in the null *scospondin*$^{icm13/icm13}$ mutant compared to wild type siblings (Figure 2-figure supplement 2A, 2B). These data show that the loss of the Reissner fiber reduces spontaneous calcium variations of ventral CSF-cNs during the critical time window for body axis straightening. On the contrary, the sparse spontaneous calcium transients in dorsal CSF-cNs were not affected by the absence of the Reissner fiber in both *scospondin* alleles (Figure 2-figure supplement 2C, 2D).

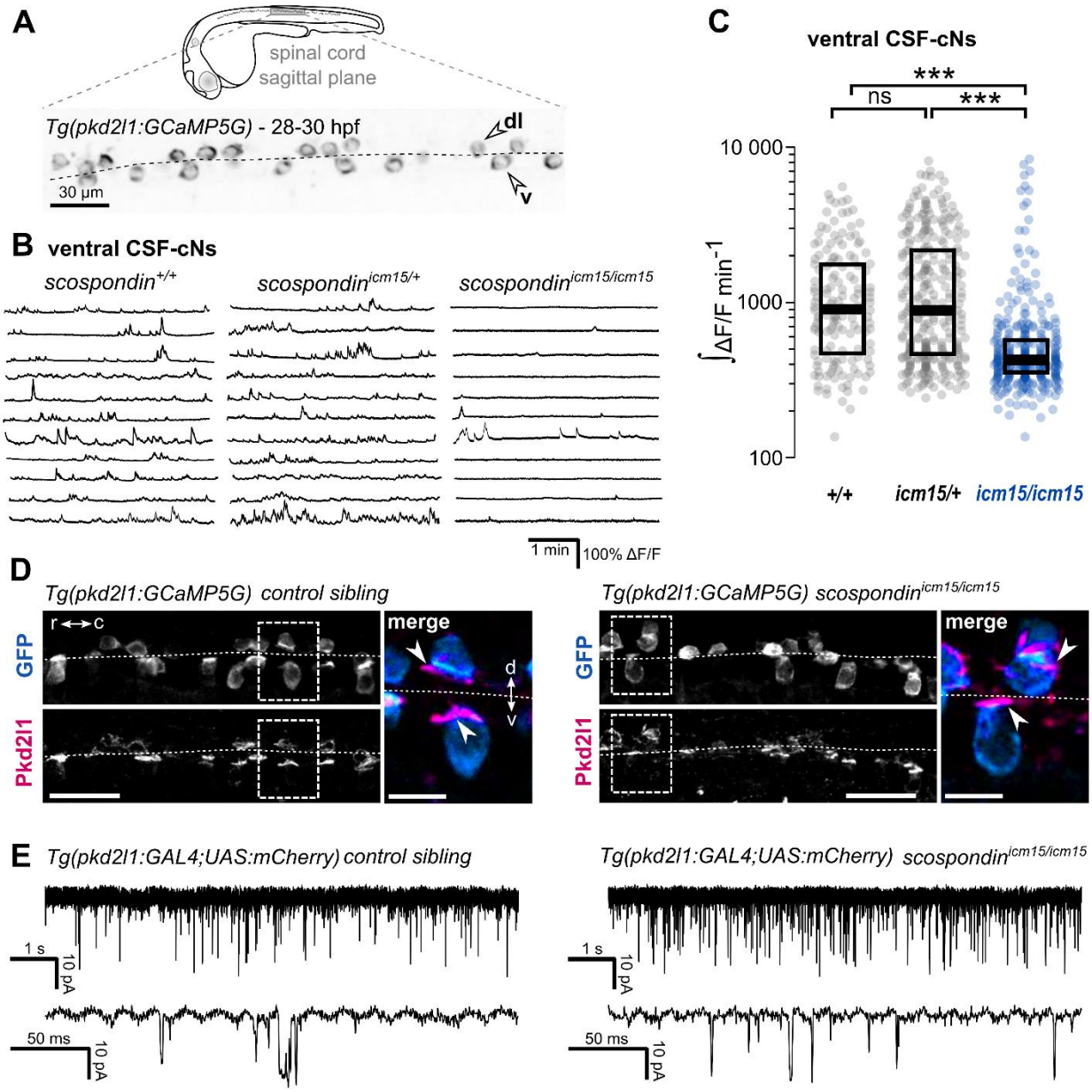

Figure 2. The Reissner fiber is required for the spontaneous calcium variations of ventral CSF-contacting neurons.

(**A**) 28-30 hpf embryos expressing the GCaMP5G calcium reporter in CSF-contacting neurons were imaged on the lateral side. *Tg(pkd2l1:GCaMP5G)* embryos label both dorso-lateral (dl, above the dotted line) and ventral (v, below the dotted line) CSF-contacting neurons (arrowheads). Scale bar: 30 µm. (**B**) Representative traces of calcium variations in individual ventral CSF-contacting neurons in wild type (*scospondin*$^{+/+}$), heterozygous (*scospondin*$^{icm15/+}$) and *scospondin*$^{icm15/icm15}$ mutants. Sample traces from individual cells with integral ΔF/F values ranging around the median distribution of the imaged population are represented for each genotype (n = 11 cells). (**C**) Quantification of the normalized integrated calcium variation over time of ventral CSF-contacting neurons in wild type (+/+), heterozygous (*icm15*/+) and *scospondin*$^{icm15/icm15}$ mutants (*icm15/icm15*, blue). Data were collected

from 5 independent experiments and include 10 wild type embryos (n=146 cells), 20 heterozygous embryos (n=287 cells) and 21 *scospondin*$^{icm15/icm15}$ mutants (n=307 cells). Each point represents a single cell. Bottom and top edges of the boxes indicate the 1st and 3rd quartiles. Bold lines represent the median value for each distribution. ns p>0.05, *** p<0.001 (Kolmogorov-Smirnov test). (**D**) Immunohistochemistry for Pkd2l1 (magenta) and GFP (blue) in *Tg(pkd2l1:GCaMP5G)* embryos at 30 hpf in the spinal cord of a control sibling (left) and *scospondin*$^{icm15/icm15}$ mutant (right). Scale bar: 30 µm. Magnification of the area delineated by dotted line boxes is represented for each condition (r: rostral, c: caudal, d: dorsal, v: ventral). Scale bar: 10 µm. *scospondin*$^{icm15/icm15}$ embryos show a similar localization of the Pkd2l1 protein at the developing apical extension (arrowheads) of the CSF-cNs (labeled by the GFP antibody, blue) compared to control siblings. (**E**) *In vivo* voltage-clamp recordings from CSF-contacting neurons in the *Tg(pkd2l1:GAL4;UAS:mCherry)* line at 30 hpf in control embryos (left) and *scospondin*$^{icm15/icm15}$ mutants (right). Note the extensive number of events in both conditions (top traces). Bottom traces represent higher temporal magnifications and allow distinguishing single channel openings.
See also Figure Supplement 1 and Video 1.

Early calcium transients in CSF-cNs require the non-selective cationic channels permeable Pkd2l1 channel *in vivo* (Sternberg et al., 2018) that is permeable to calcium ions. The reduction in calcium activity when the Reissner fiber is lacking could therefore be due to a defect in the Pkd2l1 channel localization or opening probability. *In toto* immunohistochemistry for Pkd2l1 protein showed that this channel is enriched at the differentiating apical extension of CSF-cNs in curled-down *scospondin*$^{icm15/icm15}$ mutants as well as in control embryos (Figure 2D). In order to assess Pkd2l1 channel properties, we performed *in vivo* whole cell voltage clamp recordings in double transgenic *Tg(pkd2l1:GAL4;UAS:mCherry)* embryos. In the absence of a Reissner fiber in *scospondin*$^{icm15/icm15}$ mutants, we observed spontaneous Pkd2l1 channel openings that were similar to control embryos (Figure 2E). Thus, the loss of the Reissner fiber decreases CSF-cNs intracellular calcium variations without preventing the opening nor the localization of Pkd2l1 channels in the differentiating apical extension of the cells. Altogether, these data suggest that the Reissner fiber is required for a signal acting on ventral CSF-cNs that controls both the spontaneous calcium variations and the expression of *urp2* in the embryo.

Loss of *urp2* expression is only observed in mutants devoid of the Reissner fiber, independently of calcium variations in CSF-cNs

As the Reissner fiber is required for both ventral CSF-cNs spontaneous calcium transients and *urp2* gene expression, we tested whether intracellular calcium variations are necessary for a normal *urp2* expression and axis straightness. We took advantage of the

pkd2l1$^{icm02/icm02}$ mutant where the embryonic activity of CSF-cNs is abolished (Sternberg et al., 2018).

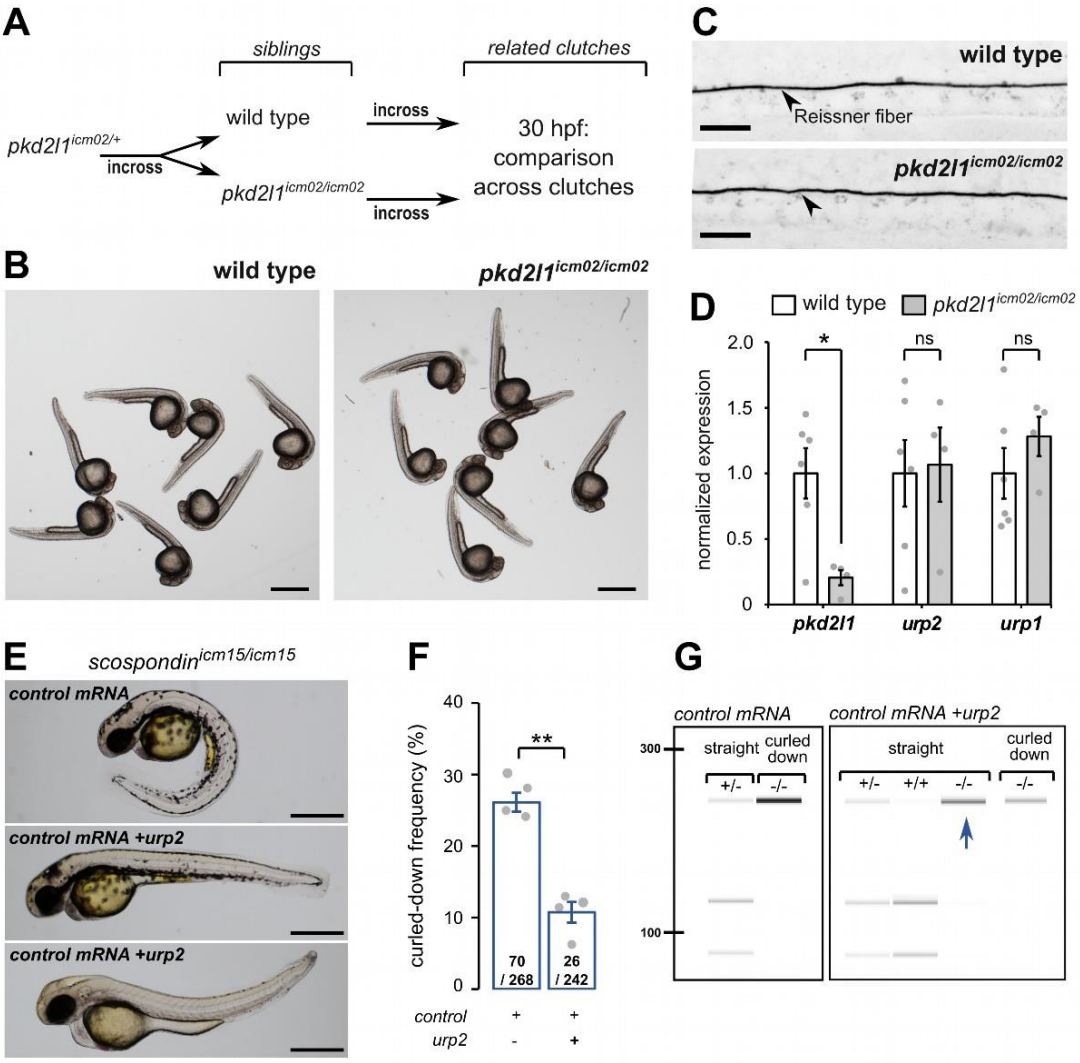

Figure 3. *urp2* expression is Pkd2l1-independent and is important for the Reissner fiber-dependent straightening of the embryonic posterior axis.

(**A**) Adult wild type and *pkd2l1*$^{icm02/icm02}$ siblings were incrossed to generate related clutches that were analyzed at 30 hpf. (**B**) Representative pictures of wild type (left) and *pkd2l1*$^{icm02/icm02}$ embryos (right) at 30 hpf. Note that mutant embryos develop a straight posterior axis. Scale bar: 0.5 mm. (**C**) Representative immunohistochemistry for the Reissner fiber imaged from the spinal cord of a wild type (top, one representative embryo out of 20) and a *pkd2l1*$^{icm02/icm02}$ embryo (bottom, one representative embryo out of 20). Note that the Reissner fiber forms properly in the mutant. Scale bars: 10 µm. (**D**) qRT-PCR analysis of mRNA levels of *pkd2l1*, *urp2* and *urp1* in wild type (white) and *pkd2l1*$^{icm02/icm02}$ embryos (grey). Data are represented as mean ± SEM. N = 6 independent replicates for wild-type and 4 for *pkd2l1*$^{icm02/icm02}$. Each point represents a single experimental replicate. ns p>0.05, * p<0.05 (unpaired t-test). (**E**) Representative pictures of *scospondin*$^{icm15/icm15}$ mutant embryos at 48 hpf after

one cell stage injections of a control mRNA alone or of a mix containing a control mRNA and *urp2* mRNA (middle and bottom). Note that upon control injections, *scospondin*$^{icm15/icm15}$ mutants display at typical curled-down phenotype, while *urp2* overexpression can lead to straightened (middle) or slightly curled-up posterior axis (bottom). Scale bar: 0.5 mm. (**F**) Quantification at 48 hpf of curled-down frequency in embryos obtained from *scospondin*$^{icm15/+}$ incrosses upon control mRNA injections (n=70 curled-down animals out of 268) or *urp2* mRNA overexpression (26 curled-down embryos out of 242). Data were collected from 4 independent clutches and represented as mean ±SEM. ** p<0.01 (paired t-test). (**G**) Injected embryos were genotyped at 48 hpf based on the loss of a restriction site in the *scospondin* mutant allele leading to a band resistant to digestion (-/-). While mutant animals are exclusively curled-down in control conditions, *urp2* mRNA overexpression leads to the detection of mutant animals displaying a straight body axis (blue arrow).
See also Figure supplement 1.

Thanks to the viability of *pkd2l1*$^{icm02/icm02}$ zygotic mutants, we generated genetically-related clutches that were either fully wild type or fully maternal & zygotic (MZ) homozygous mutant (Figure 3A). We observed that *pkd2l1*$^{icm02/icm02}$ MZ mutant embryos did not display any defect in body axis morphogenesis and were morphologically undistinguishable from wild type embryos (Figure 3B). Using immunohistochemistry, we observed that *pkd2l1*$^{icm02/icm02}$ mutants form a normal Reissner fiber in the central canal of the spinal cord at 30 hpf (Figure 3C). Next, using qRT-PCR, we tested whether *urp1* and *urp2* gene expression levels were diminished by the absence of calcium transients in CSF-cNs (Figure 3D). As the mutation in the *icm02* allele generates a premature stop codon in the *pkd2l1* gene (Böhm et al., 2016), one can predict that the *pkd2l1* mRNA would be degraded by nonsense-mediated decay. Indeed, mutant clutches displayed a 4.9 fold decrease in *pkd2l1* transcripts level compared to wild type counterparts (Figure 3D). Interestingly, we observed that *urp2* and *urp1* gene expression were not decreased in *pkd2l1*$^{icm02/icm02}$ embryos compared to wild types (Figure 3D). Altogether, these data show that the loss of Pkd2l1-driven calcium transients in CSF-cNs does not lead to a decreased expression of *urp1* and *urp2* transcripts, rejecting the hypothesis of a direct requirement for *urp2* expression of Pkd2l1-dependent intracellular calcium variations. Instead, our results show a strict correlation between the presence of the Reissner fiber, a normal *urp2* expression level and the proper morphogenesis of the embryonic body axis. Altogether, our results prompted us to hypothesize that the aberrant posterior axis curvature in absence of the Reissner fiber is a consequence of the decreased *urp2* expression.

urp2 expression in the absence of the Reissner Fiber can restore posterior axis defects

Given the strict correlation between *urp2* expression and body axis straightening, we hypothesized that restoring *urp2* levels would rescue the posterior axis curvature developed by *scospondin*$^{icm15/icm15}$ mutants. To test this hypothesis, we performed one cell stage *urp2* mRNA injections on clutches obtained from *scospondin*$^{icm15/+}$ parents. We sorted the injected embryos at 48 hpf into two morphological categories: curled-down and non-curled-down (Figure 3E, 3F). In the four independent experiments conducted, injections with a control mRNA led to a proportion of curled-down embryos close to 25%, as expected (Figure 3F). On the contrary, embryos overexpressing *urp2* showed much lower proportions of curled-down embryos (10.7 ± 1.5%; mean ±SEM; Figure 3F), suggesting that some homozygous mutants are rescued in this condition. To confirm this rescue, we genotyped curled-down and non-curled-down 48 hpf embryos injected with a control mRNA or *urp2* mRNA (Figure 3E, 3G, Figure3-figure supplement 1). As expected, wild type and heterozygous embryos injected with the control mRNA displayed a straight body axis, while *scospondin*$^{icm15/icm15}$ showed a downward curvature of the posterior axis. Instead, *urp2* overexpression lead to detect straight or slightly curled-up *scospondin*$^{icm15/icm15}$ embryos at several instances (Figure 3E, 3G, Figure3-figure supplement 1). Thus, restoring higher *urp2* levels is sufficient to prevent the embryonic posterior axis defects in *scospondin* mutants. These observations confirm that *urp2* neuropeptide expressed in CSF-cNs may signal at long range, as suggested from the expression of the receptor in dorsal somites (Zhang 2018), to ensure a proper axis morphogenesis.

Epinephrine and norepinephrine restore morphogenesis of the posterior axis and *urp* expression in *scospondin* mutants

Based on our observations, we assumed that the Reissner fiber is necessary for the activity of at least one signaling pathway regulating *urp2* gene expression together with body axis morphogenesis. Epinephrine and norepinephrine belong to the monoamine neurotransmitter family and are known to bind the Reissner fiber in rats (Caprile et al., 2003) and frogs (Diederen et al., 1983). Recently, systemic bath applications of monoamines have been described to rescue body axis defects in curled-down cilia defective mutants (Lu et al., 2020, (Zhang et al., 2018). We investigated the possible role of epinephrine and norepinephrine in the regulation of the RF signaling pathways.

First, we tested if epinephrine and norepinephrine could influence the curled-down phenotype developed by *scospondin*$^{icm15/icm15}$ mutants. We compared sibling animals generated from incrosses of *scospondin*$^{icm15/+}$. We first analyzed the effect of 2.5 hours bath applications of epinephrine and norepinephrine on control embryos at 30 hpf (Figure 4A). Epinephrine and norepinephrine have a moderate impact on the shape of the head-to-tail

axis of initially straight embryos, which display a slight curled-up phenotype after exposure to monoamines (Figure 4B). To estimate the straightness of the posterior axis, we quantified the angle formed between the ear, the caudal limit of the yolk extension and the tip of the tail (Figure 4C, top panel). This angle is distributed around 190.6° in control embryos exposed to a vehicle solution (median value; Figure 4C, bottom left graph). Comparatively, control embryos exposed to monoamines exhibit a distribution of ear-to-tail angles shifted towards slightly higher values (median values: 220.4° and 213.6° for epinephrine and norepinephrine, respectively; Figure 4C, bottom right graph). Next, we analyzed the effect of epinephrine and norepinephrine on *scospondin*$^{icm15/icm15}$ embryos. While mutant animals exposed to a vehicle solution display a typical curled-down body axis, *scospondin*$^{icm15/icm15}$ mutants treated with monoamines exhibit a reduction in the downward curvature of the posterior axis (Figure 4B). Quantifications of ear-to-tail angles in *scospondin*$^{icm15/icm15}$ mutants show a large increase of the median angle value after exposure to monoamines, compared to embryos treated with a vehicle solution (106.5° for vehicle, 167.1° for epinephrine and 158.5° for norepinephrine; median values; Figure 4C). Altogether, these data show that epinephrine and norepinephrine can partially restore the posterior axis geometry of *scospondin*$^{icm15/icm15}$ mutants, suggesting that monoamines can rescue the Reissner fiber-dependent signal required for a straight embryonic body axis.

Next, we analyzed the effect of epinephrine and norepinephrine on *urp1* and *urp2* gene expression using qRT-PCR. In control siblings, *urp1* expression remains comparable after vehicle, epinephrine or norepinephrine exposure (Figure 4D). Consistently with our previous results, *urp1* expression is not significantly modified in curled-down *scospondin*$^{icm15/icm15}$ embryos compared to their control siblings receiving the same treatment (1.01 +/- 0.17 fold change; mean ± SEM; Figure 4D). However, we observed a slight increase of *urp1* expression in curled-down mutant embryos treated with epinephrine and norepinephrine compared to vehicle treatment (1.58 ± 0.43 and 1.28 ± 0.23 fold changes for epinephrine and norepinephrine respectively; mean ± SEM). As expected, *urp2* expression level is significantly decreased in curled-down *scospondin*$^{icm15/icm15}$ mutants compared to straight siblings (0.22 ± 0.06 fold change; mean ± SEM; Figure 4E). Epinephrine and norepinephrine treatments also do not change *urp2* expression in control siblings, but significantly increase it in curled-down homozygous mutant embryos (7.42 ± 4,23 and 4.67 ± 1.15 fold changes for epinephrine and norepinephrine respectively; mean ±SEM; Figure 4E).

These observations show that the rescue of the posterior axis curvature of *scospondin* homozygous mutant embryos by monoamines is associated with an increase of the expression of *urp1* and *urp2* neuropeptides. Epinephrine and norepinephrine compensate the loss of the Reissner fiber both on Urotensin-II-related neuropeptides

366 expression and on posterior axis curvature, suggesting that these compounds act on the
367 Reissner fiber-dependent signaling pathway in the embryonic CSF.

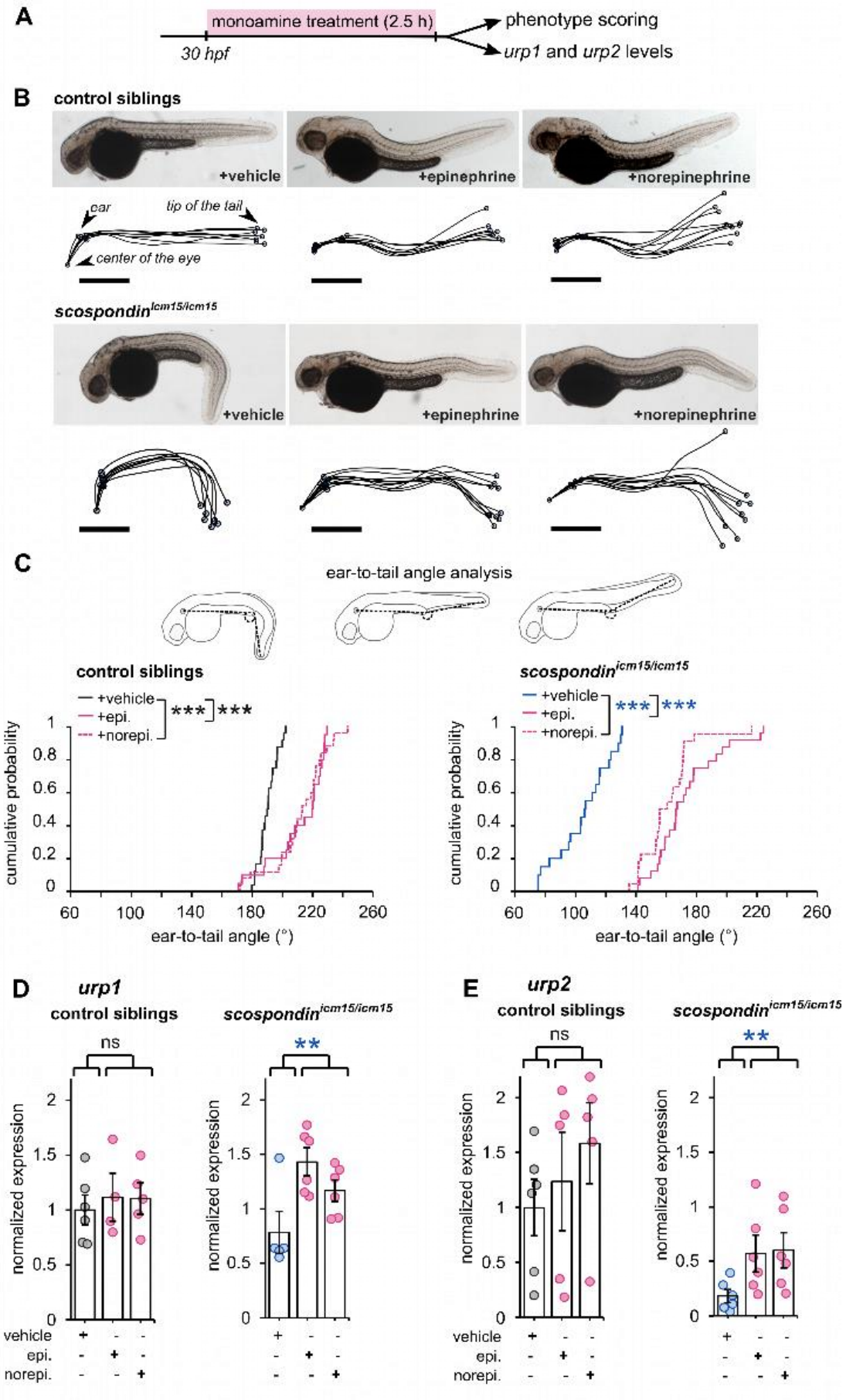
A
monoamine treatment (2.5 h)
30 hpf
phenotype scoring
urp1 and urp2 levels
B
control siblings
+vehicle
+epinephrine
+norepinephrine
ear
tip of the tail
center of the eye
scospondin icm15/icm15
+vehicle
+epinephrine
+norepinephrine
C
ear-to-tail angle analysis
control siblings
scospondin icm15/icm15
+vehicle
+epi.
+norepi.
***
***
cumulative probability
ear-to-tail angle (°)
D
urp1
control siblings
scospondin icm15/icm15
ns
**
normalized expression
vehicle
epi.
norepi.
E
urp2
control siblings
scospondin icm15/icm15
ns
**
normalized expression

Figure 4. Epinephrine and norepinephrine compensate the loss of the Reissner fiber for body axis straightening and increase *urp* expression.

(**A**) Curled-down *scospondin*$^{icm15/icm15}$ mutants and their control siblings were sorted at 30 hpf according to the geometry of their posterior axis and then exposed to a E3 solution (vehicle), epinephrine or norepinephrine for 2.5 hours prior to phenotype scoring and RNA extraction. (**B**) Representative pictures of control siblings (top) and *scospondin*$^{icm15/icm15}$ mutants (bottom) after vehicle (left), epinephrine (middle) or norepinephrine (right) treatments. For each condition, the global morphologies of treated embryos are represented by superimposed traces linking the center of the eye, the ear and the tip of the tail in one representative clutch. Scale bar: 0.5 mm. (**C**) Quantification of the angle formed between the ear, the caudal limit of the yolk extension and the tip of the tail (as shown on the schematics, top) in control siblings (bottom left) and *scospondin*$^{icm15/icm15}$ mutants (bottom right). Data were collected from 3 independent experiments and include 24, 20, 25 control siblings treated with a vehicle solution, epinephrine, norepinephrine respectively (black, solid pink and dotted pink line respectively) and 20, 24, 22 *scospondin*$^{icm15/icm15}$ embryos treated with a vehicle solution, epinephrine, norepinephrine respectively (blue, solid pink and dotted pink line respectively) *** p<0.001 (Kolmogorov-Smirnov test). (**D**, **E**) qRT-PCR analysis of the mRNA level of *urp1* (**D**) and *urp2* (**E**) in control siblings (left) and *scospondin*$^{icm15/icm15}$ embryos (right). Data are represented as mean ± SEM. n=4 to 6 independent replicates for each condition. Each point represents a single experimental replicate. ns p>0.05, ** p<0.01 (GLM test).

Epinephrine and norepinephrine restore the Reissner fiber-dependent calcium signaling in ventral CSF-cNs of *scospondin* mutants

The Reissner fiber is required for three concomitant events: intracellular calcium variations and *urp2* expression in ventral CSF-cNs, and the straightening of the posterior axis. We therefore asked whether the delivery of monoamines in CSF could also restore calcium variations in ventral CSF-cNs. To address this question, we performed hindbrain ventricle injections of epinephrine or norepinephrine in the *Tg(pkd2l1:GCaMP5G); scospondin*^{icm15} *embryos* at 30 hpf, and recorded calcium variations in ventral CSF-cNs within the spinal cord 20 to 60 minutes after the injections (Figure 5A). In order to assess how the monoamines used diffuse in the central canal of the spinal cord and whether they are stable enough in the CSF, we performed immunostainings against norepinephrine 30 and 60 minutes after hindbrain ventricle injections (Figure 5- figure supplement 1). We observed an abundant norepinephrine-positive signal in the central canal of the rostral most region of the spinal cord 30 minutes post-injection, and the median and caudal most-regions 60 minutes post injection, which was absent in control injections (Figure 5- figure supplement 1). This observation indicates that norepinephrine diffuses down the central canal when injected in the same conditions used for *in vivo* calcium imaging and that it is stable in the CSF after an

hour, in agreement with former results in the mammalian ventricular system of dogs (Maas and Landis, 1965), sheeps (Forbes and Baile, 1974) and rats (Fuxe and Ungerstedt, 1966; Levitt et al., 1983).

We first analyzed the effect of epinephrine and norepinephrine injections on control embryos displaying a straight body axis at 30 hpf and observed that an exogenous delivery of monoamines did not influence the basal calcium variations of ventral CSF-cNs (Figure 5B, 5D). Next, we analyzed the effect of epinephrine and norepinephrine in *scospondin*$^{icm15/icm15}$ mutants (Figure 5C, 5E, Figure5-video 1). As described previously, ventral CSF-cNs displayed a 44.1% decrease of calcium variations in *scospondin*$^{icm15/icm15}$ embryos compared to control siblings in control condition with vehicle injections (median value; Figure 5D, 5E), confirming

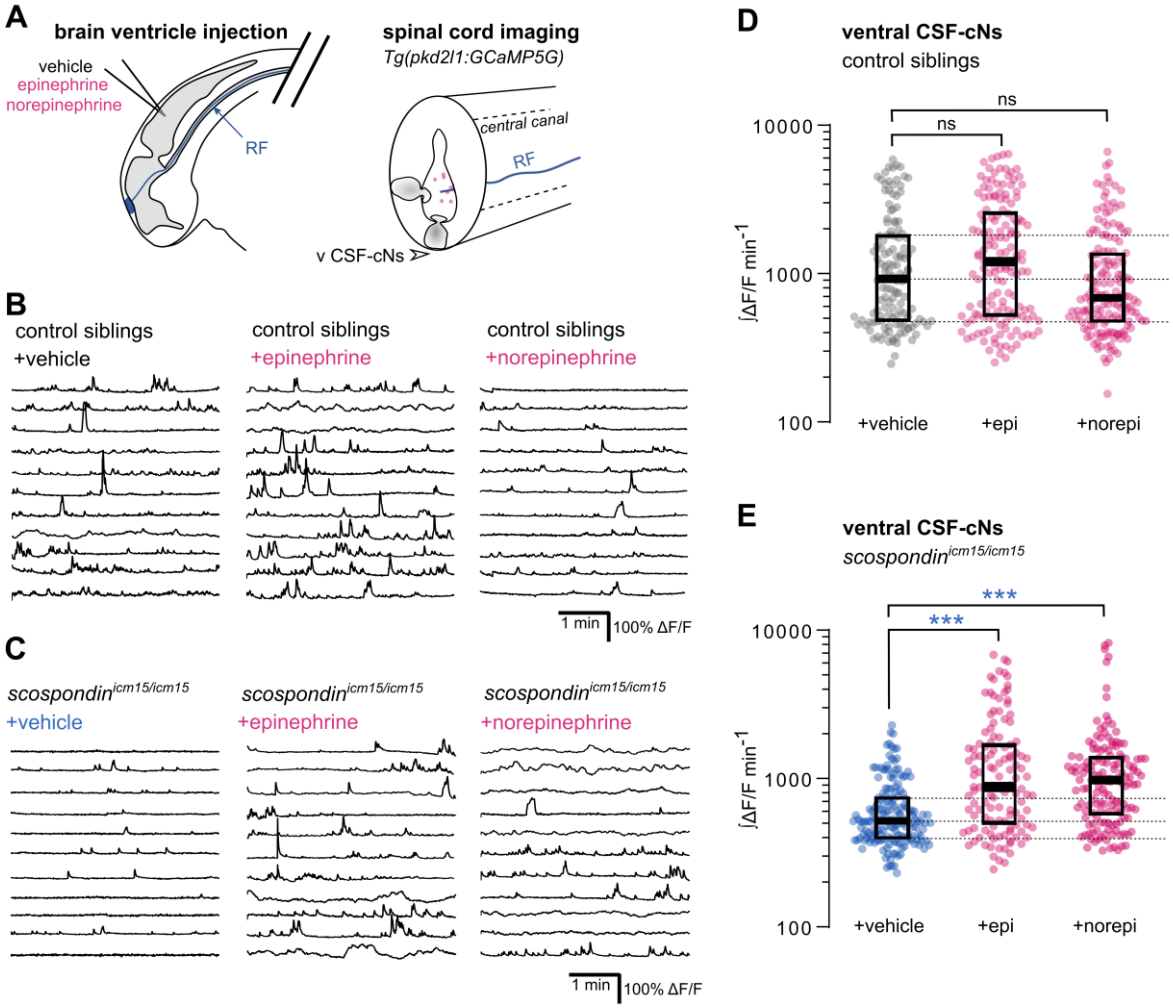

Figure 5. Local monoamine delivery restores calcium variations of ventral CSF-contacting neurons in *scospondin* mutants.

(**A**) *Tg(pkd2l1:GCaMP5G)* embryos we used to perform hindbrain ventricle injections at 30 hpf of artificial CSF (vehicle), epinephrine or norepinephrine (left). Intracellular calcium variations in ventral CSF-contacting neurons (v CSF-cNs, arrowhead) were recorded in the spinal cord 30 minutes after the injection to allow monoamines (pink dots) diffusing down the central can where bathes the

Reissner fiber (RF) in control embryos. (**B**, **C**) Representative traces of calcium variations of individual ventral CSF-contacting neurons in control siblings (**B**) and *scospondin*$^{icm15/icm15}$ mutants (**C**) after vehicle (left), epinephrine (middle) and norepinephrine injections (right). Sample traces from individual cells with integral ΔF/F values ranging around the median distribution of the imaged population are represented for each condition (n=11). (**D**, **E**) Quantification of the normalized integrated intracellular calcium variation over time of ventral CSF-contacting neurons in control siblings (**D**) and *scospondin*$^{icm15/icm15}$ mutants (**E**). Data were collected from 3 independent experiments and include 9, 11 and 12 control embryos recorded after vehicle, epinephrine and norepinephrine injections respectively (n=131, 150 and 164 cells respectively) and 11, 10 and 10 *scospondin*$^{icm15/icm15}$ mutants after vehicle, epinephrine and norepinephrine injections respectively (n=168, 124 and 150 cells respectively). Each point represents a single cell. Bottom and top edges of the boxes indicate the 1st and 3rd quartiles. Dotted lines represent the distribution range around the 1st and 3rd quartiles of control embryos injected with a vehicle solution. Bold lines represent the median value for each distribution. ns p>0.05, *** p<0.001 (Kolmogorov-Smirnov test).
See also Figure supplement 1 and Video 1.

the observations reported in Figure 3. Interestingly, injections of epinephrine or norepinephrine in *scospondin*$^{icm15/icm15}$ mutants increased the median $\int$ΔF/F min^{-1} by 70.02% and 88.6% respectively compared to vehicle injections (Figure 5E). Moreover, the rescue of the spontaneous activity of CSF-cNs by monoamines in mutant embryos reached comparable levels to those observed in control siblings (Figure 5D-E). These data show that epinephrine and norepinephrine restore the Reissner fiber-dependent calcium transients in ventral CSF-cNs in *scospondin* mutants.

Altogether, our results are compatible with the existence of a signal that links the Reissner fiber to both *urp2* expression and calcium variations in ventral CSF-cNs that can be modulated by monoaminergic activation. These observations suggest that endogenous epinephrine and norepinephrine may act locally to tune calcium signaling in CSF-cNs.

Norepinephrine can be detected in the embryonic CSF and adrenergic receptors are expressed by spinal cells contacting the CSF

To assess that this modulation takes place at the interface between CSF and the cells lining the central canal, we performed immunostainings against endogenous norepinephrine at 30 hpf in *Tg(scospondin-GFP)* embryos labeling *in vivo* the Reissner fiber (Troutwine et al., 2019). As previously described, SCO-spondin positive material in the CSF contributes mainly to form the fiber, but is also present as punctated material in close vicinity the fiber, referred to here as extrafibrillar material, (Troutwine et al., 2019, Figure 6A). We observed norepinephrine positive puncta colocalized with the Reissner fiber as well as endogenous norepinephrine positive signals following patterns similar to extrafibrillar material labelled by

462 the *Tg(scospondin-GFP)* transgene. This can also be observed closely at the level of the
463 *massa caudalis*, formed by the accumulation of SCO-spondin at the caudal end of the central
464 canal (Figure 6A). These observations suggest that norepinephrine is endogenously present
465 in the embryonic CSF where it is associated with the Reissner-positive material in the central
466 canal.

467 To address the question of the receptor associated to this signaling, we performed
468 immunostainings against the adrenergic receptor Adrb2, binding both epinephrine and
469 norepinephrine, which is described to be transiently expressed in the zebrafish nervous
470 system at early stages of embryonic life (Wang et al., 2009). We observed that Adrb2 is
471 distributed ventrally in the neural tube, at the interface with the central canal, in a pattern that
472 suggests a membrane localization in both control siblings and *scospondin*$^{icm15/icm15}$ mutants
473 (Figure 6B). Thus, Adrb2 localization is suitable for binding endogenous ligands present in
474 the CSF.

475 Next, we addressed the question of whether Adrb2 is expressed in CSF-contacting
476 neurons, which could explain the rescue of calcium transients observed in
477 *scospondin*$^{icm15/icm15}$ mutants after epinephrine and norepinephrine injections. Double
478 immunostainings against Adrb2 and GFP in *Tg(pkd2l1:GCaMP5G)* control siblings show that
479 both signals cover different domains in the ventral most region of the spinal cord (Figure 6C),
480 where the Adrb2 positive domain remains in the ventral midline, inserted between two rows
481 of ventral CSF-contacting neurons (Figure 6-video 1). As ventral CSF-contacting neurons are
482 known to derive from lateral floor plate progenitors (Park et al., 2004; Yang et al., 2010), the
483 medial cells expressing Adrb2 most probably correspond to the medial floor plate.
484 Importantly, the same distribution is observed in *scospondin*$^{icm15/icm15}$ mutants (Figure 6C and
485 Figure 6-video 1). This observation suggests that the loss of calcium signaling in
486 *scospondin*$^{icm15/icm15}$ mutants is unlikely due to a defect in the Adrb2 distribution in the spinal
487 cord.

488 Altogether, our results indicate that endogenous adrenergic signals could modulate
489 the Reissner fiber-dependent signaling pathway that instructs body axis straightening during
490 embryonic development, and suggests that monoamines act on CSF-contacting neurons
491 through an indirect mechanism.

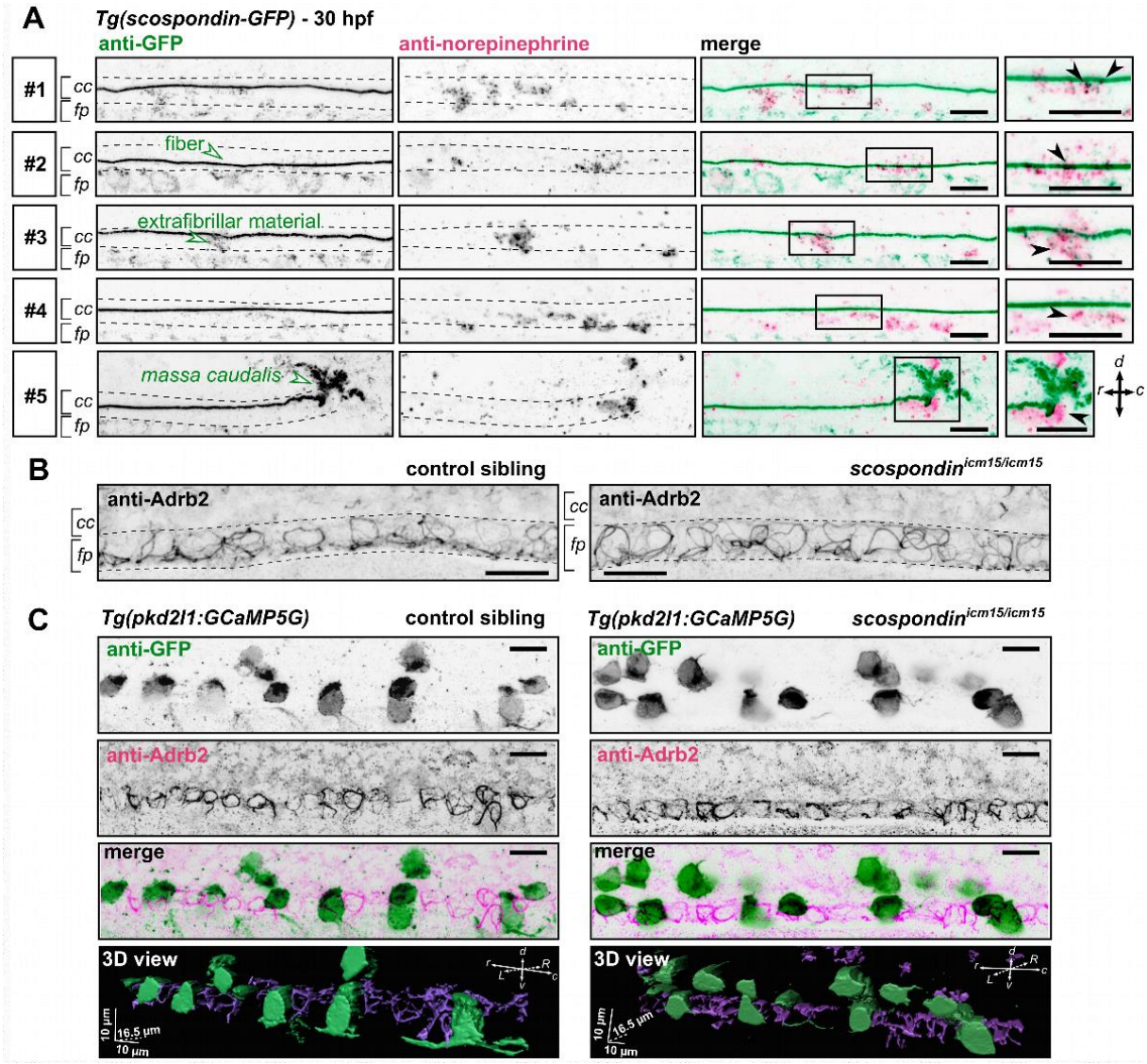

Figure 6. The adrenergic receptor Adrb2 is expressed in cells ventral to the central canal in which norepinephrine can be detected.

(**A**) Double immunodetection of GFP (left) and endogenous norepinephrine (middle) in the spinal cord of *Tg(scospondin-GFP)* embryos at 30 hpf imaged laterally. Merged signals and close up of boxed regions are represented on the right. 5 representative examples (#1 to #5) out of 26 embryos are shown (no signal was detected in 6 embryos out of 26 in total, n=2 independent experiments). In the central canal, norepinephrine positive signals can be detected as colocalized with the Reissner fiber itself (black arrowheads; embryos #1, 2, 3), with extrafibrillar material in the central canal (black arrowheads; embryos #4 and #5), and closely apposed to the *massa caudalis* located after the caudal limit of the central canal (black arrowhead; embryo #6). Scale bars: 10 µm. r: rostral; c: caudal; d: dorsal; v: ventral; cc: central canal; fp: floor plate. (**B**) Immunohistochemistry for the adrenergic receptor Adrb2 in a 30 hpf control sibling (left, representative example out of 8 embryos) and a *scospondin*$^{icm15/icm15}$ embryo (right, representative example out of 9 embryos). Adrb2 is distributed along the midline of the ventral most region of the neural tube (corresponding to the floor plate, fp) at the interface with the central canal (cc). Embryos are oriented rostral to the left and dorsal to the top. Scale bars: 10 µm. (**C**) Sagittal views of double immunostainings against GFP and Adrb2 in the spinal

cord of *Tg(pkd2l1:GCaMP5G)* embryos at 30 hpf. Maximal z-projections are shown for a control sibling (left; one embryo out of 12) and a *scospondin*$^{icm15/icm15}$ mutant (right; one embryo out of 8). Merged signals show that GFP positive and Adrb2 positive signals cover different domains in the ventral most region of the neural tube. 3D reconstructions of the same field of views (bottom panel: GFP: green; Adrb2: purple) further illustrate that Adrb2 is enriched in a distinct cell population that is medial to ventral CSF-contacting neurons. Scale bars: 10 µm. L: left; R: right;

See also Video 1.

Discussion

Using a combination of transcriptomic analyses together with *in vivo* calcium imaging and pharmacology, we show here that the Reissner fiber is essential for signaling to the developing CSF-contacting neurons (CSF-cNs). In these neurons, the Reissner fiber is required for both *urp2* expression and spontaneous intracellular calcium variations. This functional interaction between the Reissner fiber and ventral CSF-cNs is required for a normal curvature of the developing posterior axis of zebrafish. Using monoamine injections into the CSF, we show that the CSF-cNs response to the signal from the Reissner fiber can be modulated by local adrenergic activation *in vivo,* suggesting that the Reissner fiber acts by controlling the availability of a chemical signal in the CSF.

urp2 expression in ventral CSF-cNs depends on the presence of the Reissner fiber and impacts on the curvature of embryonic axis

Previous results in both cilia-defective and *scospondin* mutants suggested that mutants that fail to form a Reissner fiber display a strong downregulation of both Urotensin-II-related neuropeptides 1 and 2 in the embryo (Lu et al., 2020; Rose et al., 2020; Zhang et al., 2018). Our new results contradict the observation that *urp1* is downregulated in *scospondin* mutants (Lu et al., 2020). In the present study, our transcriptomic analysis of *scospondin* mutants yielded surprisingly few candidates commonly misregulated in the two alleles, and *urp2* was the only gene with a strong downregulation, while *urp1* showed no significant change. We confirmed this result by qRT-PCR and showed again that only *urp2* is strongly downregulated, while *urp1* transcripts levels were not significantly affected. In line with our results, the investigation of a newly generated *scospondin* hypomorphic allele (Rose et al., 2020) also revealed *urp2* as the major downregulated gene in homozygous mutant and did not report a *urp1* downregulation.

We further show that *urp2* overexpression in *scospondin* mutants decreases the frequency of curled-down phenotypes, confirming that *urp2* expression level is involved in the control of embryonic axis curvature (Lu et al., 2020; Zhang et al., 2018). However, *urp2* may not be the only determinant of embryonic axis morphogenesis downstream of the Reissner fiber, as single *urp2* morpholino knockdown do not show a defective axis curvature (Zhang et al., 2018). Parallel signaling pathways that would likely act post-transcriptionally and would therefore not be detected using our transcriptomic strategy may be involved.

The discovery of a new hypomorphic allele for *scospondin* recently revealed an inflammatory signature induced by the loss of the Reissner fiber at the embryonic stage (Rose et al., 2020). In our work, we did not detect such a signature in our transcriptomic analysis (see Figure 1-table supplement 1). We can speculate that these differences are due

552 to difference in the fish genetic background or husbandry conditions. Our work therefore
553 begs for further studies in order to decipher the molecular pathways downstream and/or in
554 parallel to Urp2 that regulate the morphogenesis of the embryonic axis.
555

556 **Intracellular calcium variations in developing ventral CSF-cNs require the Reissner**
557 **fiber**

558 In the embryo, ventral CSF-cNs are spontaneously active via the opening of the Pkd2l1
559 calcium channel enriched at the level of the developing apical extension of the cells
560 (Sternberg et al., 2018). In addition to controlling *urp2* gene expression in CSF-cNs, we
561 report here that the Reissner fiber is also required for calcium signaling in *urp2*-expressing
562 cells. By investigating the *pkd2l1* mutant deprived of calcium signaling in embryonic CSF-
563 cNs, our work rejects the simple explanation that the Reissner fiber controls *urp2* mRNA
564 level and axis straightness by increasing calcium intracellular concentrations in CSF-cNs.
565 Indeed, the absence of *urp* genes downregulation observed in the *pkd2l1* mutant compared
566 to wild-type goes against this hypothesis.
567 One question remaining is how the Reissner Fiber controls calcium variations in ventral
568 CSF-cNs. We recently showed that the Reissner fiber is functionally coupled to the
569 mechano-sensory function of these interoceptive neurons in the larva (Orts-Del'Immagine et
570 al., 2020). However, embryonic CSF-cNs are not fully differentiated, as they do not harbor a
571 fully developed apical extension known to tune their mechanosensory function at larval stage
572 (Desban et al., 2019). We therefore favor the hypothesis that the Reissner fiber acts via the
573 modulation of the CSF content, which is supported by the restoration of calcium signaling in
574 CSF-cNs upon monoamine injections in the brain ventricles.
575

576 **Adrenergic activation restores the Reissner fiber-dependent signaling and axis**
577 **straightening**

578 Earlier reports suggest that the Reissner fiber can interact with different neuro-
579 modulators, including monoamines (Caprile et al., 2003; Diederen et al., 1983). Monoamines
580 globally supplied in the fish water were also found to rescue body curvature in Reissner fiber-
581 defective mutants (Lu et al., 2020; Zhang et al., 2018). They are therefore good candidates
582 to influence the Reissner fiber signal towards ventral CSF-cNs. We added to previous report
583 (Lu et al., 2020) that the action of both epinephrine and norepinephrine can compensate
584 locally, directly in the ventricular cavities, for the loss of the Reissner fiber on calcium
585 signaling. We also used quantitative PCR to confirm the regulation of *urp* neuropeptides
586 expression by both epinephrine and norepinephrine in *scospondin* mutants, extending the
587 previous result obtained using *in situ* hybridization after epinephrine treatments (Lu et al,

2020). These two monoamines rescue the *scospondin* phenotype for three features: spontaneous calcium variations and Urotensin-II-related peptides expression in CSF-cNs, and body axis curvature.

One possible interpretation of our results is that the Reissner fiber is essential for the control of endogenous epinephrine and norepinephrine distribution in the embryonic CSF. This is consistent with our immunodetection of norepinephrine in close vicinity with the Reissner fiber in the embryonic central canal. This hypothesis is supported by the presence of noradrenergic neurons in the embryonic hindbrain as early as 24 hpf (Holzschuh et al., 2003), providing a potential source of monoamines that would need to be transported caudally to the central canal of the spinal cord. This hypothesis is reinforced by our original result showing the localization of the Adrb2 receptor at the interface with CSF in the ventral part of the neural tube, ideally located to bind norepinephrine ligands that we found distributed close to Reissner-positive material. Interestingly Adrb2 belongs to the G protein-coupled receptors family and was identified to trigger cytoplasmic calcium raise *in vitro* (Galaz-Montoya et al., 2017). In zebrafish, the adrenergic system plays important roles in the control of wakefulness (Singh et al., 2015) and of cardiac contractions (Steele et al., 2011). However, no morphological defects have been reported in animal missing the rate-limiting enzyme for the synthesis of epinephrine and norepinephrine (Singh et al., 2015). This might reflect the masking of the phenotype due to transcriptional adaptation to the genetic mutation (Rossi et al., 2015). Alternatively, redundant signaling pathways might mask the role of monoamines in axis curvature control. Nonetheless, our results support the idea that the cross-talk between the Reissner fiber and undifferentiated CSF-cNs is likely to be of chemical nature, possibly through monoamines themselves. They further support the idea that monoamines act on CSF-cNs in an indirect manner. Future investigations will allow to fully delineate the contribution and mechanism of action of endogenous monoamines on ventral CSF-cNs signaling and body axis curvature.

Altogether, our study unravels a signal from the Reissner fiber to the developing CSF-contacting neurons. We also show that adrenergic activation can modulate this signal during embryonic body axis morphogenesis. Interestingly, a temporally controlled inactivation of cilia motility leads to spine curves reminiscent of adolescent idiopathic scoliosis (Grimes et al., 2016). Recent results suggest that, as in the embryo, the Reissner fiber and Urp reception in slow muscles are also implicated in the maintenance of a straight spine during postembryonic development (Lu et al., 2020; Rose et al., 2020; Troutwine et al., 2019; Zhang et al., 2018). Our work will pave the way for future investigations to identify the potential of

623 the interplay between CSF-cNs and the adrenergic system to modulate the Reissner fiber-
624 dependent morphogenesis of the spine in the juvenile.

625 **Material and Methods**

626 **Key resources table**

Key Resources Table				
Reagent type (species) or resource	**Designation**	**Source or reference**	**Identifiers**	**Additional information**
Genetic reagent (*D. rerio*)	*scospondin*^{icm13}	(Cantaut-Belarif et al., 2018)	ZFIN : ZDB-ALT-181113-3	
Genetic reagent (*D. rerio*)	*scospondin*^{icm15}	(Cantaut-Belarif et al., 2018)	ZFIN: ZDB-ALT-181113-4	
Genetic reagent (*D. rerio*)	*pkd2l1*^{icm02}	(Böhm et al., 2016)	ZFIN : ZDB-ALT-160119-6	
Genetic reagent (*D. rerio*)	*Tg(pkd2l1:GCaMP5G)*^{icm07Tg}	(Böhm et al., 2016)	ZFIN: ZDB-ALT-160119-4	
Genetic reagent (*D. rerio*)	*Tg(pkd2l1:GAL4)*^{icm10Tg}	(Fidelin et al., 2015)	ZFIN: ZBD-ALT-150324-1	
Genetic reagent (*D. rerio*)	*Tg(UAS:mCherry)*	(Robles et al., 2014)	ZFIN: ZBD-ALT-130702-1	
Genetic reagent (*D. rerio*)	*Tg(scospondin-GFP)*	(Troutwine et al., 2019)		R. S. Gray lab
Recombinant DNA reagent	*pCS2-urp2* plasmid	G. Pézeron, this work		Used for RNA synthesis
Recombinant DNA reagent	*pCS2-Ras-eGFP* plasmid	(Ségalen et al., 2010)		Used for RNA synthesis

Sequence-based reagent	URP2_BamHI_F gcgcgcGGATCCgtatctgtagaatctgctttgctgc	This work		forward oligonucleotide used for *urp2* cloning
Sequence-based reagent	URP2_XbaI_R gcgcgcTCTAGAggcagagggtcagtcgtgttat	This work		reverse oligonucleotide used for *urp2* cloning
Sequence-based reagent	*urp2* forward: CCACCGGATCACCATCATTACC	This work		qPCR oligonucleotide
Sequence-based reagent	*urp2* reverse: GATGCCACCGCTGTCTATAGTG	This work		qPCR oligonucleotide
Sequence-based reagent	*urp1* forward: TGCGCTGCCTCTGTATTCAG	This work		qPCR oligonucleotide
Sequence-based reagent	*urp1* reverse: CTTTGTCCGTCTTCAACCTCTG	This work		qPCR oligonucleotide
Sequence-based reagent	*pkd2l1* forward: GCGAACTATGCCCAATGAGG	This work		qPCR oligonucleotide
Sequence-based reagent	*pkd2l1* reverse: TCTCAAAGCTGTTCCCCACA	This work		qPCR oligonucleotide
Sequence-based reagent	*lsm12b* forward: GAGACTCCTCCTCCTCTAGCAT	This work		qPCR oligonucleotide
Sequence-based reagent	*lsm12b* reverse: GATTGCATAGGCTTGGGACAAC	This work		qPCR oligonucleotide
Antibody	Anti-Reissner fiber, rabbit , polyclonal	(Didier et al., 1995)	Courtesy of S. Gobron	Dilution 1:200

Antibody	Anti-GFP, chicken, polyclonal	Abcam, Cat# ab13970	RRID:AB_300798	Dilution 1:500
Antibody	Anti-Pkd2l1, rabbit, polyclonal	(Sternberg et al., 2018)		Dilution 1:200
Antibody	Anti-Norepinephrine, rabbit, polyclonal	Millipore, Cat# AB120	RRID:AB_90481	Dilution 1:100
Antibody	Anti-Adrb2, rabbit, polyclonal	ThermoFischer Scientific, Cat# PA5-80323	RRID:AB_2787652	Dilution 1:200
Antibody	Alexa Fluor-488 goat anti chicken IgG (H+L)	Molecular Probes, Cat# A-11039	RRID:AB_142924	Dilution 1:500
Antibody	Alexa Fluor-568 goat anti-rabbit IgG (H+L)	Molecular Probes, Cat# A-11036	RRID:AB_10563566	Dilution 1:500
Antibody	Alexa Fluor-488 donkey anti rabbit IgG (H+L)	Molecular Probes, Cat# A-21206	RRID:AB_2535792	Dilution 1:500
Chemical compound, drug	DL-Norepinephrine hydrochloride	Sigma	Cat# A7256	Dilution to 3mM
Chemical compound, drug	+- Epinephrine hydrochloride	Sigma	Cat# E4642	Dilution to 3mM
Chemical compound, drug	MS 222	Sigma	Cat# E10521	Dilution to 0.2% w/v
Chemical compound, drug	alpha-bungarotoxin	Tocris	Cat# 2133	Dilution to 500 µM
Software, algorithm	MATLAB	MathWorks	RRID:SCR_001622	
Software, algorithm	Prism	GraphPad	RRID:SCR_002798	

Software, algorithm	Fiji	(Schindelin et al., 2012)	RRID:SCR_002285	
Software, algorithm	Imaris	Oxford Instruments	RRID:SCR_007370	

627

628

629 **Animal husbandry and genotyping**

630 All procedures were performed on zebrafish embryos between 30 and 48 hpf in accordance
631 with the European Communities Council Directive (2010/63/EU) and French law (87/848)
632 and approved by the Paris Brain Institute (Institut du Cerveau) and the French Ministery for
633 research (APAFIS agreement 2018071217081175). All experiments were performed on
634 *Danio rerio* embryos of AB, Tüpfel long fin (TL) and nacre background. Animals were raised
635 at 28.5°C under a 14/10 light/dark cycle until the start of the experiment. Genotyping was
636 performed as previously described for *scospondin*^{icm13} and *scospondin*^{icm15} (Cantaut-Belarif et
637 al., 2018) and *pkd2l1*^{icm02} (Böhm et al., 2016).

638

639 **RNA sample preparation**

640 For each experiment, condition (developmental time point and pharmacological treatment)
641 and phenotype (either straight or curled-down), 30 sibling embryos were sorted in
642 independent vials. After euthanasia in 0.2% MS 222 (Sigma, E10521), embryos were
643 resuspended in 1 mL of Trizol™ (ThermoFischer Scientific, 15596026) and dissociated by
644 multiple aspirations through the needle of a syringe. 200 µL chloroform were added prior to
645 centrifugation and extraction of the aqueous phase. Nucleic acids were precipitated using
646 700 µL isopropanol, and the pellet was resuspended in 200 µL water. RNAs were purified
647 using the RNeasy Micro Kit (Qiagen, 74004), following the provider's instruction. We
648 performed the optional on-column DNAse treatment to improve RNAs purity. RNAs were
649 eluted in 30 µL water to ensure a high concentration, and the quality and quantity of the
650 extract was evaluated on a TapeStation System® (Agilent).

651

652 **RNA sequencing analysis**

653 mRNA library preparation was realized following manufacturer's recommendations (KAPA
654 mRNA HyperPrep Kit, Roche). Final samples pooled library preparations were sequenced on
655 Nextseq 500 ILLUMINA, corresponding to 2x30 millions of 75 base pair reads per sample
656 after demultiplexing. Quality of raw data was evaluated with FastQC (Andrews et al., 2010).

Poor quality sequences was trimmed or removed using Trimmomatic software (Bolger et al., 2014) to retain only good quality paired reads. Star v2.5.3a (Dobin et al., 2013) was used to align reads on GRCz11 reference genome using standard options. Quantification of gene and isoform abundances was achived using with Rsem 1.2.28, prior to normalization with the edgeR bioconductor package (Robinson et al., 2009). Finally, differential analysis was conducted with the GLM framework likelihood ratio test from edgeR.

The quality control and PCA analysis (not shown) indicated that one sample was not reaching the same reproducibility as the two others, even after trimming and normalization. We therefore used the average value of the two most reliable replicates to calculate the average expression level (count per million, cpm) of all the 28 214 genes either in straight controls or in curled-down embryos (average of the expression in the two alleles *icm13* and *icm15*). We then filtered out low-expression genes that had an expression level below 1 c.p.m. in the average of the straight control replicates. We then kept genes that had an average fold change between curled embryos and controls of 0.75 for down-regulated genes (120 genes), and 1.45 for up-regulated genes (94 genes). We turned back to the original raw cpm values of the three replicates in the two alleles for these two short-lists. We tested the consistency of the fold change across replicates and across alleles with a general linear model (GLM) (Nelder et al., 1972). The design matrix included 2 regressors of interest (encoding whether the sample is a straight control or curled embryos) and 2 confounding variables (the unwanted variability that might be associated with the two different genetic environments of the two families of fish carrying the *icm13* and the *icm15* allele). Statistical significance of the effect of interest (above and beyond confounding factors) was tested using a t-test. Because of the potential false discovery associated with multiple testing, we then used the Benjamini–Hochberg procedure (Benjamini, et al., 1995).

Potential genes of interest were sorted according to their increasing p-values. To shorten the list of potential genes of interest, we determined at which rank i the p-value became higher than the Benjamini–Hochberg criterion using (i / total nb)* 0.2. This method allows for up to 20% of false-positives, but avoids the rejection of true-positives that was manifest with a more stringent correction as the Bonferroni correction. For example, the *scospondin* mRNA level in the *icm13* allele is highly decreased, presumably through non-sense mediated decay: the Bonferroni correction would have rejected this result as not significant, whereas the Benjamini–Hochberg procedure keeps it in the list of potentially interesting genes (see Figure 1-Source Data 1 for the complete lists). However, this procedure requires a post-hoc validation with an independent technique for each potential gene of interest, as we did by qRT-PCR (see below).

693 **Quantitative RT-PCR**

694 1.2 µg of each RNA sample was retro-transcribed using the Verso cDNA Synthesis Kit
695 (ThermoFischer Scientific, AB1453B) following the provider's instructions. A 1:3 ratio of
696 random hexamer:polydT primers was used to favor mRNA amplification without a strong bias
697 for the 3' end of messengers. qPCR experiments were performed using the LightCycler® 480
698 SYBR Green I Master kit (Roche, 04707516001) on a LightCycler® 96 machine (Roche).
699 Each pair of primers (see Key Resource Table) was tested beforehand on a given cDNA
700 stock that was diluted in a series of 4 points. Linearity of CT variation with the cDNA dilution
701 as well as single peaks in the melting curves corresponding to single amplicons were
702 assessed. For each new RNA extraction, we tested that no amplification was detectable
703 when the PCR was performed directly on the RNA stock (-RT). We used the housekeeping
704 gene *lsm12b* as an internal reference in each experiment. qPCRs were repeated two to three
705 times for each cDNA stock and the average CT was used for further calculations. The
706 relative abundance of the gene of interest was evaluated using the CT comparison formula:
707 $2e^{-\Delta CT}$. All results were obtained on at least three biological replicates (except for *pkd2l1*
708 mutant extracts), each originating from a single mating.
709

710 **Monitoring of body axis curvature in developing embryos**

711 To characterize the exact evolution of the geometry of the posterior axis in
712 *scospondin*$^{icm15/icm15}$ mutants during the early stages on embryogenesis (Figure supplement
713 1), we performed incrosses of *scospondin*$^{icm15/+}$ parents. Eggs were collected 30 minutes
714 after mating and maintained at 28.5°C until 19.5 hpf. Embryos were staged according to
715 (Kimmel et al., 1995) at 19.5 hpf. Individual embryos were mounted laterally at 20 hpf in
716 1.5% low-melting point agarose, imaged using a AZ100M macroscope (Nikon), unmounted
717 and kept at 28.5°C until they were remounted for the next stages (22, 24, 28 and 30 hpf).
718 The time window necessary for mounting-imaging-unmounting at each step was short
719 enough (10-15 min) to be neglected.
720

721 **Pharmacology and quantification of body axis curvature**

722 30 hpf embryos from *scospondin*$^{icm15/+}$ incrosses were treated during 2.5 hours at 28.5°C with
723 E3 medium alone (vehicle), epinephrine hydrochloride (Sigma, E4642) or norepinephrine
724 hydrochloride (Sigma, A7256) both diluted to 3 mM in E3 medium (Figure 4). To avoid light-
725 induced oxidation of epinephrine and norepinephrine, dishes were covered with foil paper
726 during the incubation time. To ensure a proper quantification of ear-to-tail angles, embryos
727 were then fixed over-night in 4% PFA 6-well plates, rinsed 3 times during 45 minutes in 1X
728 PBS, mounted laterally in 1.5% low-melting point agarose and imaged using a AZ100M

macroscope (Nikon). For each embryo, the angle between the ear, the caudal limit of the yolk extension and the tip of the tail (Figure 4C) was quantified using Fiji (Schindelin et al., 2012). Representative traces of the global morphology of the embryos after treatment were drawn for all experimental conditions on one representative clutch (Figure 4B) by linking the center of the eye to the ear and following the dorsal line linking somite boundaries until the tip of the tail.

In vivo **calcium imaging**

Tg(pkd2l1:GCaMP5G) embryos were manually dechorionated at 30 hpf, mounted laterally in 1.5% low-melting point agarose, and paralyzed by injecting 1-2 nL of 500 µM alpha-bungarotoxin (Tocris, 2133) in the caudal muscles of the trunk. When required (Figure 5), hindbrain ventricle injections were performed using artificial cerebrospinal fluid (aCSF, containing in mM: 134 NaCl, 2.9 KCl, 1.2 $MgCl_2$, 10 HEPES, 10 glucose and 2.1 $CaCl_2$; 290 $mOsm.kg^{-1}$, adjusted to pH 7.7–7.8 with NaOH) as a vehicle solution. Epinephrine hydrochloride (Sigma, E4642) and norepinephrine hydrochloride (Sigma, A7256) were diluted to 3 mM in aCSF before hindbrain ventricle injections, using a sharp funnel shape needle with an approximate tip diameter of 1-3 µm. Embryos were imaged 20 to 60 minutes after hindbrain ventricle injections. Calcium imaging was performed at 4 Hz using a spinning disk confocal microscope (Intelligent Imaging Systems, Denver) for 4 minutes. Imaging was restricted to the region of the spinal cord located above the yolk extension. Regions of interest were manually selected based on an average projection of the time-lapse and according to the dorso-ventral position of the cells. The integrals of normalized ΔF/F signals were calculated using a custom script on MATLAB (see full description in (Sternberg et al., 2018)). The MATLAB codes used for data analysis are available at Github https://github.com/wyartlab/Cantaut-Belarif-et-al.-2020.

In vivo **patch clamp recording**

Whole-cell recordings were performed in aCSF on 30 hpf double transgenic *Tg(pkd2l1:GAL4;UAS:mCherry)* embryos carrying the *scospondin*^{icm15} mutation and their respective control siblings. Embryos were pinned through the notochord with 0.025 mm diameter tungsten pins. Skin and muscle from two to three segments around segment 10 were dissected out using a glass suction pipette. A MultiClamp 700B amplifier, a Digidata series 1440 A Digitizer, and pClamp 10.3 software (Axon Instruments, Molecular Devices, San Jose, California, USA) were used for acquisition. Raw signals were acquired at 50 kHz and low-pass filtered at 10 kHz. Patch pipettes (1B150F-4, WPI) with a tip resistance of 6–8MΩ were filled with internal solution containing in mM: K-gluconate 115, KCl 15, MgCl2 2, Mg-ATP 4, HEPES-

765 free acid 10, EGTA 5 or 10, 290 mOsm/L, pH adjusted to 7.2 with KOH with Alexa 488 at 40 µM
766 final concentration). Holding potential was − 85 mV, away from the calculated chloride reversal
767 potential (E_{Cl} = - 51 mV).
768

769 **Immunohistochemistry and confocal imaging**

770 Embryos were manually dechorionated and euthanized using 0.2% MS 222 (Sigma,
771 E10521) prior to fixation.

772 To detect the Pkd2l1 channel together with GFP (Figure 2D), 30 hpf embryos were
773 fixed 4 hours at 4°C in 4% PFA and then washed 3 times during 30 minutes in 1X PBS.
774 Embryos were blocked overnight at 4°C in a solution containing 0.7% Triton, 1% DMSO and
775 10% NGS. The primary antibodies were incubated overnight at 4°C in a solution containing
776 0.5% Triton, 1% DMSO and 1% NGS and subsequently washed 4 times during 1 hour in a
777 solution containing 0.5% Triton and 1% DMSO (washing solution). Secondary antibodies
778 were incubated 3 hours at room temperature in a solution containing 0.5% Triton, 1% DMSO
779 and 1% NGS. The mix of secondary antibodies was centrifuged 10 minutes at 10 000 rpm
780 prior to the incubation to pellet unconjugated dyes (supernatant only was used for the
781 incubation). Embryos were then washed 4 times during 2 hours using the washing solution
782 and thereafter overnight at 4°C in 1X PBS.

783 To detect the Reissner fiber (Figure 3C), 30 hpf embryos were fixed 4 hours at 4°C in
784 4% PFA and washed 3 times during 30 minutes in 1X PBS. Embryos were then blocked
785 overnight in a solution containing 0.5% Triton, 1% DMSO and 10% NGS. The primary
786 antibody was diluted in a solution containing 0.5% Triton, 1% DMSO and 1% NGS and
787 incubated overnight at 4°C. Embryos were subsequently washed 4 times during 1 hour in a
788 solution containing 0.5% Triton and 1% DMSO (washing solution). Secondary antibodies
789 were incubated 3 hours at room temperature in a solution containing 0.5% Triton, 1% DMSO
790 and 1% NGS. The mix of secondary antibodies was centrifuged 10 minutes at 10 000 rpm
791 prior to the incubation to pellet unconjugated dyes (supernatant only was used for the
792 incubation). Embryos were subsequently washed 4 times during 2 hours using the washing
793 solution and thereafter overnight at 4°C in 1X PBS.

794 To detect exogenous (Figure Supplement 4) and endogenous (Figure 5A)
795 norepinephrine alone (Figure Supplement 4) or together with GFP (Figure 5A), we used an
796 antibody designed against a Glutaraldehyde-conjugated form of norepinephrine (Millipore,
797 AB120). Thus, 30 hpf embryos were fixed 1.5 hour at 4°C under agitation in a 4% PFA-
798 0.125% Glutaraldehyde-3% sucrose solution to allow reactivity. Embryos were then washed
799 3 times in 1X PBS during 30 minutes and the yolks and skin from rostral parts of the trunk

were removed. Embryos were blocked overnight at 4°C in a solution containing 0.6% Triton, 1.2% DMSO and 10% normal goat serum (NGS). An additional blocking step was performed during 3 hours at room temperature the day after. Primary antibodies were incubated in a solution containing 1% Triton, 1% DMSO and 1% NGS during one day at room temperature plus one night at 4°C. Embryos were then washed extensively 4 times during 2 hours in a solution containing 0.5% Triton and 1% DMSO (washing solution). Secondary antibodies were incubated 3 hours at room temperature in a solution containing 1% Triton, 1% DMSO and 1% NGS. The mix of secondary antibodies was centrifuged 10 minutes at 10 000 rpm prior to the incubation to pellet unconjugated dyes (supernatant only was used for the incubation). Embryos were subsequently washed 4 times during 2 hours using the washing solution, 4 times during 1 hour using a solution of 50% washing solution-50% 1X PBS and thereafter overnight at 4°C in 1X PBS.

To detect Adrb2 alone (Figure 6B) or together with GFP (Figure 6C), embryos were fixed 2 hours at 4°C in a 4% PFA-3% sucrose solution and washed 3 times in 1X PBS during 30 minutes. The yolks and the skin from the rostral part of the trunk were removed and embryos were blocked overnight in a solution containing 0.6% Triton, 1.2% DMSO and 10% normal goat serum (NGS). Primary antibodies were incubated at 4°C during 2 days in a solution containing 1% Triton, 1% DMSO and 1% NGS. Embryos were washed extensively 4 times during 2 hours in a solution containing 0.5% Triton and 1% DMSO (washing solution). Secondary antibodies were incubated 3 hours at room temperature in a solution containing 1% Triton, 1% DMSO and 1% NGS. The mix of secondary antibodies was centrifuged 10 minutes at 10 000 rpm prior to the incubation to pellet unconjugated dyes (supernatant only was used for the incubation). Embryos were subsequently washed using the washing solution 4 times during 2 hours, 4 times during 1 hour using a solution of 50% washing solution-50% 1X PBS and thereafter washed in 1X PBS overnight at 4°C.

The following dilutions of primary antibodies were used: rabbit anti-Reissner fiber 1:200 (Didier et al., 1995), rabbit anti-Pkd2l1 1:200 (Sternberg et al., 2018), chicken anti-GFP 1:500 (Abcam ab139170), rabbit anti-norepinephrine 1:100 (Millipore, AB120), rabbit anti-Adrb2 1:200 (ThermoFischer Scientific, PA5-80323). All secondary antibodies were from Molecular Probes© and used at 1:500. Systematic omission of the primary antibody confirmed the specificity of the immunostaining results. Zebrafish embryos were mounted laterally in Vectashield® Antifade Mounting Medium (Clinisciences, H1000) and imaged on an inverted SP8 DLS confocal microscope (Leica). Images were then processed using Fiji (Schindelin et al., 2012). Maximal Z-projections of 6-9 microns in depth are represented in Figure 2D and Figure 3C, 9-12 microns in depth in Figure 6A, 6B and Figure Supplement 4B and 18-22 microns in Figure 6C. 3D views shown in Figure 6C were obtained using Imaris.

836

837 **RNA microinjections**

838 To produce mRNA, *urp2* CDS was amplified from cDNA by PCR and cloned (BamHI - XbaI)
839 into pCS2+. Messenger RNA were produced with the mMESSAGE mMACHINE™ kit
840 (Ambion™). 1 nL RNA-containing solution was injected into 1- to 2-cell stage embryos
841 obtained from *scospondin*$^{icm15/+}$ incrosses. Each clutch was separated into three groups:
842 uninjected and injected either with a control mRNA (100 ng / µL, *ras-eGFP* encoding for a
843 membrane tagged GFP, (Ségalen et al., 2010) or with a mix containing control mRNA and
844 *urp2* mRNA (100 ng / µL total, 1:1 ratio). To assess for injection quality, GFP-positive
845 embryos were first sorted out at 1 dpf and then scored at 48 hpf for body axis curvature
846 defects.

847

848 **Statistics**

849 All values are represented as boxplots (median ± interquartile range) or mean ± SEM (stated
850 for each in the figure legend). All statistics were performed using MATLAB and Excel. In the
851 figure panels, asterisks denote the statistical significance calculated using the appropriate
852 test (stated for each test in the legends): *, $p<0.05$; **, $p<0.01$; ***, $p<0.001$; ns, $p>0.05$.

Acknowledgements

We gratefully thank Prof. Ryan S. Gray for providing us with *Tg(scospondin-GFP)* embryos, Prof. Sylvie Schneider-Maunoury and Dr. Christine Vesque for providing us the Ras-eGFP plasmid, Dr. Stephane Gobron for the antibody directed against the Reissner fiber. We thank Monica Dicu and Antoine Arneau for fish care, the ICM.Quant imaging facility for instrument use, scientific and technical assistance and François-Xavier Lejeune for advice on statistics. This work benefited from equipment and services from the iGenSeq (RNA sequencing) and iCONICS (RNAseq analysis) core facilities at the ICM (Institut du Cerveau, Hôpital Pitié-Salpétrière, PARIS, France). We thank for critical feedback all members of the Wyart lab (www.wyartlab.com). This work was supported by, the HFSP Program Grants #RGP0063/2018, the Fondation Schlumberger pour l'Education et la Recherche (FSER/2017) for C.W, and the Fondation des Treilles for Y.C.B. The research leading to these results has received funding from the program "Investissements d'avenir" ANR-10-IAIHU-06 (Big Brain Theory ICM Program) and ANR-11-INBS-0011 – NeurATRIS: Translational Research Infrastructure for Biotherapies in Neurosciences.

References

Andrews S. 2010. FastQC: a quality control tool for high throughput sequence data. *Bioinformatics*. Available at: http://www.bioinformatics.babraham.ac.uk/projects/fastqc/

Benjamini Y, Hochberg Y. 1995. Controlling the false discovery rate: a practical and powerful approach to multiple testing. *J. Roy. Stat. Soc*. **57(1)**: 289–300

Berg DA, Belnoue L, Song H, Simon A. 2013. Neurotransmitter-mediated control of neurogenesis in the adult vertebrate brain. *Development* **140**: 2548–2561. https://doi.org/10.1242/dev.088005

Böhm UL, Prendergast A, Djenoune L, Figueiredo SN, Gomez J, Stokes C, Kaiser S, Suster M, Kawakami K, Charpentier M, Concordet JP, Rio JP, Del Bene F, Wyart C. 2016. CSF-contacting neurons regulate locomotion by relaying mechanical stimuli to spinal circuits. *Nat Commun* **7**:1–8. doi:10.1038/ncomms10866

Bolger AM, Lohse M, Usadel B. 2014. Trimmomatic: A flexible trimmer for Illumina sequence data. *Bioinformatics* **30**:2114–2120. doi:10.1093/bioinformatics/btu170

Brand M, Heisenberg CP, Warga RM, Pelegri F, Karlstrom RO, Beuchle D, Picker A, Jiang YJ, Furutani-Seiki M, van Eeden FJ, Granato M, Haffter P, Hammerschmidt M, Kane D a, Kelsh RN, Mullins MC, Odenthal J, Nüsslein-Volhard C. 1996. Mutations affecting development of the midline and general body shape during zebrafish embryogenesis. *Development* **123**:129–142.

Cantaut-Belarif Y, Sternberg JR, Thouvenin O, Wyart C, Bardet PL. 2018. The Reissner Fiber in the Cerebrospinal Fluid Controls Morphogenesis of the Body Axis. *Curr Biol* **28**:2479-2486.e4. doi:10.1016/j.cub.2018.05.079

Caprile T, Hein S, Rodríguez S, Montecinos H, Rodríguez E. 2003. Reissner fiber binds and transports away monoamines present in the cerebrospinal fluid. *Mol Brain Res* **110**:177–192. doi:10.1016/S0169-328X(02)00565-X

Chan CJ, Heisenberg CP, Hiiragi T. 2017. Coordination of Morphogenesis and Cell-Fate Specification in Development. *Curr Biol* **27**:R1024–R1035. doi:10.1016/j.cub.2017.07.010

Desban L, Prendergast A, Roussel J, Rosello M, Geny D, Wyart C, Bardet PL. 2019. Regulation of the apical extension morphogenesis tunes the mechanosensory response of microvilliated neurons. *PLoS Biol* **17**:1–27. doi:10.1371/journal.pbio.3000235

Didier R, Dastugue B, Meniel A. 1995. The secretory material of the subcommissural organ of the chick embryo. Characterization of a specific polypeptide by two-dimensional electrophoresis. *Int J Dev Biol* **39**:493–499.

Diederen JHB, Vullings HGB, Rombout JHWM, de Gunst-Schoonderwoerd ATM. 1983. The Subcommissural Organ-Liquor Fibre Complex: the Binding of Catecholamines to the Liquor Fibre in Frogs of the Rana esculenta Complex. *Acta Zool* **64**:47–53. doi:10.1111/j.1463-6395.1983.tb00641.x

Djenoune L, Desban L, Gomez J, Sternberg JR, Prendergast A, Langui D, Quan FB, Marnas H, Auer TO, Rio JP, Del Bene F, Bardet PL, Wyart C. 2017. The dual developmental origin of spinal cerebrospinal fluid-contacting neurons gives rise to distinct functional subtypes. *Sci Rep* **7**:1–14. doi:10.1038/s41598-017-00350-1

Dobin A, Davis CA, Schlesinger F, Drenkow J, Zaleski C, Jha S, Batut P, Chaisson M, Gingeras TR. 2013. STAR: Ultrafast universal RNA-seq aligner. *Bioinformatics* **29**:15–21. doi:10.1093/bioinformatics/bts635

Fame RM, Lehtinen MK. 2020. Emergence and Developmental Roles of the Cerebrospinal Fluid System. *Dev Cell* **52**:261–275. doi:10.1016/j.devcel.2020.01.027

Faubel R, Westendorf C, Bodenschatz E, Eichele G. 2016. Cilia-based flow network in the brain ventricles. *Science (80-)* **353**:176–178. doi:10.1126/science.aae0450

Fidelin K, Djenoune L, Stokes C, Prendergast A, Gomez J, Baradel A, Del Bene F, Wyart C. 2015. State-dependent modulation of locomotion by GABAergic spinal sensory neurons. *Curr Biol* **25**:3035–3047. doi:10.1016/j.cub.2015.09.070

Forbes JM, Baile CA. 1974. Norepinephrine Diffusion from Hypothalamus to Cerebrospinal Fluid and Cerebrospinal Fluid to Hypothalamus of Sheep. *J Dairy Sci* **57**:826–832. doi:10.3168/jds.S0022-0302(74)84971-4

Fuxe K, Ungerstedt U. 1966. Localization of catecholamine uptake in rat brain after intraventricular injection. *Life Sci* **5**:1817–1824. doi:10.1016/0024-3205(66)90058-0

Galaz-Montoya M, Wright SJ, Rodriguez GJ, Lichtarge O, Wensel TG. 2017. β2-Adrenergic receptor activation mobilizes intracellular calcium via a non-canonical cAMP-independent signaling pathway. *J Biol Chem* **292**:9967–9974. doi:10.1074/jbc.M117.787119

Grimes DT, Boswell CW, Morante NFC, Henkelman RM, Burdine RD, Ciruna B. 2016. Zebrafish models of idiopathic scoliosis link cerebrospinal fluid flow defects to spine curvature. *Science (80-)* **1284**:1341–1344.

Hagenlocher C, Walentek P, M Ller C, Thumberger T, Feistel K. 2013. Ciliogenesis and cerebrospinal fluid flow in the developing Xenopus brain are regulated by foxj1. *Cilia* **2**:12. doi:10.1186/2046-2530-2-12

Holzschuh J, Barrallo-Gimeno A, Ettl AK, Knapik EW, Driever W. 2003. Noradrenergic neurons in the zebrafish hindbrain are induced by retinoic acid and require tfap2a for expression of the neurotransmitter phenotype. *Development* **130**:5741–5754. doi:10.1242/dev.00816

Jaffe KM, Grimes DT, Schottenfeld-Roames J, Werner ME, Ku TSJ, Kim SK, Pelliccia JL, Morante NFC, Mitchell BJ, Burdine RD. 2016. C21orf59/kurly Controls Both Cilia Motility and Polarization. *Cell Rep* **14**:1841–1849. doi:10.1016/j.celrep.2016.01.069

Kaiser K, Gyllborg D, Procházka J, Salašová A, Kompaníková P, Molina FL, Laguna-Goya R, Radaszkiewicz T, Harnoš J, Procházková M, Potěšil D, Barker RA, Casado ÁG, Zdráhal Z, Sedláček R, Arenas E, Villaescusa JC, Bryja V. 2019. WNT5A is transported via lipoprotein particles in the cerebrospinal fluid to regulate hindbrain morphogenesis. *Nat Commun* **10**:1–15. doi:10.1038/s41467-019-09298-4

Kimmel CB, Ballard WW, Kimmel SR, Ullmann B, Schilling TF. 1995. Stages of embryonic development of the zebrafish. *Dev Dyn* **203**:253–310. doi:10.1002/aja.1002030302

Kramer-Zucker AG, Olale F, Haycraft J, Yoder BK, Schier AF, Drummond IA. 2005. Cilia-driven fluid flow in the zebrafish pronephros, brain and Kupffer's vesicle is required for normal organogenesis. *Development* **132**:1907–1921. doi:10.1242/dev.01772

Langford MB, O'Leary CJ, Veeraval L, White A, Lanoue V, Cooper HM. 2020. WNT5a Regulates Epithelial Morphogenesis in the Developing Choroid Plexus. *Cereb Cortex* 1–15. doi:10.1093/cercor/bhz330

Lehmann C, Naumann WW. 2005. Axon pathfinding and the floor plate factor Reissner's substance in wildtype, cyclops and one-eyed pinhead mutants of Danio rerio. *Dev Brain Res* **154**:1–14. doi:10.1016/j.devbrainres.2004.09.009

Lehtinen MK, Zappaterra MW, Chen X, Yang YJ, Hill AD, Lun M, Maynard T, Gonzalez D, Kim S, Ye P, D'Ercole AJ, Wong ET, LaMantia AS, Walsh CA. 2011. The Cerebrospinal Fluid Provides a Proliferative Niche for Neural Progenitor Cells. *Neuron* **69**:893–905. doi:10.1016/j.neuron.2011.01.023

Levitt M, Kowalik S, Barkai AI. 1983. Measurement of tritiated norepinephrine metabolism in intact rat brain. *J Neurosci Methods* **8**:155–160. doi:10.1016/0165-0270(83)90116-4

Lu H, Shagirova A, Goggi JL, Yeo HL, Roy S. 2020. Reissner fibre-induced urotensin signalling from cerebrospinal fluid-contacting neurons prevents scoliosis of the vertebrate spine. doi:10.1242/bio.052027

Maas JW, Landis DH. 1965. Brain norepinephrine and behavior. A behavioral and kinetic study. *Psychosom Med* **27**:399–407. doi:10.1097/00006842-196509000-00001

Meiniel O, Meiniel R, Lalloué F, Didier R, Jauberteau MO, Meiniel A, Petit D. 2008. The lengthening of a giant protein: When, how, and why? *J Mol Evol* **66**:1–10. doi:10.1007/s00239-007-9055-3

Olstad EW, Ringers C, Hansen JN, Wens A, Brandt C, Wachten D, Yaksi E, Jurisch-Yaksi N. 2019. Ciliary Beating Compartmentalizes Cerebrospinal Fluid Flow in the Brain and Regulates Ventricular Development. *Curr Biol* **29**:229-241.e6. doi:10.1016/j.cub.2018.11.059

Orts-Del'Immagine A, Cantaut-Belarif Y, Thouvenin O, Roussel J, Baskaran A, Langui D, Koëth F, Bivas P, Lejeune FX, Bardet PL, Wyart C. 2020. Sensory Neurons Contacting the Cerebrospinal Fluid Require the Reissner Fiber to Detect Spinal Curvature In Vivo. *Curr Biol* **30**:827-839.e4. doi:10.1016/j.cub.2019.12.071

Park HC, Shin J, Appel B. 2004. Spatial and temporal regulation of ventral spinal cord precursor specification by Hedgehog signaling. *Development* **131**:5959–5969. doi:10.1242/dev.01456

Quan FB, Dubessy C, Galant S, Kenigfest NB, Djenoune L, Leprince J, Wyart C, Lihrmann I, Tostivint H. 2015. Comparative distribution and in vitro activities of the urotensin II-

related peptides URP1 and URP2 in zebrafish: Evidence for their colocalization in spinal cerebrospinal fluid-contacting neurons. *PLoS One* **10**:1–21. doi:10.1371/journal.pone.0119290

Robinson MD, McCarthy DJ, Smyth GK. 2009. edgeR: A Bioconductor package for differential expression analysis of digital gene expression data. *Bioinformatics* **26**:139–140. doi:10.1093/bioinformatics/btp616

Robles E, Laurell E, Baier H. 2014. The retinal projectome reveals brain-area-specific visual representations generated by ganglion cell diversity. *Curr Biol* **24**:2085–2096. doi:10.1016/j.cub.2014.07.080

Rose CD, Pompili D, Henke K, Harris MP, Nitz M, Ciruna B, Rose CD, Pompili D, Henke K, Gennip JLM Van, Meyer-miner A, Rana R. 2020. Report SCO-Spondin Defects and Neuroinflammation Are Conserved Mechanisms Driving Spinal Deformity across Genetic Models of Idiopathic Scoliosis Report SCO-Spondin Defects and Neuroinflammation Are Conserved Mechanisms Driving Spinal Deformity across Gene 1–11. doi:10.1016/j.cub.2020.04.020

Rossi A, Kontarakis Z, Gerri C, Nolte H, Hölper S, Krüger M, Stainier DYR. 2015. Genetic compensation induced by deleterious mutations but not gene knockdowns. *Nature* **524**:230–233. doi:10.1038/nature14580

Schindelin J, Arganda-Carreras I, Frise E, Kaynig V, Longair M, Pietzsch T, Preibisch S, Rueden C, Saalfeld S, Schmid B, Tinevez JY, White DJ, Hartenstein V, Eliceiri K, Tomancak P, Cardona A. 2012. Fiji: An open-source platform for biological-image analysis. *Nat Methods* **9**:676–682. doi:10.1038/nmeth.2019

Ségalen M, Johnston CA, Martin CA, Dumortier JG, Prehoda KE, David NB, Doe CQ, Bellaïche Y. 2010. The Fz-Dsh Planar Cell Polarity Pathway Induces Oriented Cell Division via Mud/NuMA in Drosophila and Zebrafish. *Dev Cell* **19**:740–752. doi:10.1016/j.devcel.2010.10.004

Singh C, Oikonomou G, Prober DA. 2015. Norepinephrine is required to promote wakefulness and for hypocretin-induced arousal in zebrafish. *Elife* **4**:1–22. doi:10.7554/eLife.07000.001

Steele SL, Yang X, Debiais-Thibaud M, Schwerte T, Pelster B, Ekker M, Tiberi M, Perry SF. 2011. In vivo and in vitro assessment of cardiac-adrenergic receptors in larval zebrafish (Danio rerio). *J Exp Biol* **214**:1445–1457. doi:10.1242/jeb.052803

Sternberg JR, Prendergast AE, Brosse L, Cantaut-Belarif Y, Thouvenin O, Orts-Del'Immagine A, Castillo L, Djenoune L, Kurisu S, McDearmid JR, Bardet PL, Boccara C, Okamoto H, Delmas P, Wyart C. 2018. Pkd2l1 is required for mechanoception in cerebrospinal fluid-contacting neurons and maintenance of spine curvature. *Nat Commun* **9**:1–10. doi:10.1038/s41467-018-06225-x

Sullivan-Brown J, Shottenfeld J, Okabe N, Hostetter CL, Serluca FC, Thiberge SY, Burdine RD. 2008. Zebrafish mutations affecting cilia motility share similar cystic phenotypes and suggest a mechanism of cyst formation that differs from pkd2 morphants. *Dev Biol* **314**:261–275. doi:10.1016/j.jacc.2007.01.076.White

Thouvenin O, Keiser L, Cantaut-Belarif Y, Carbo-Tano M, Verweij F, Jurisch-Yaksi N, Bardet PL, van Niel G, Gallaire F, Wyart C. 2020. Origin and role of the cerebrospinal fluid bidirectional flow in the central canal. *Elife* **9**:1–37. doi:10.7554/eLife.47699

Tostivint H, Ocampo Daza D, Bergqvist CA, Quan FB, Bougerol M, Lihrmann I, Larhammar D. 2014. Molecular evolution of GPCRs: Somatostatin/urotensin II receptors. *J Mol Endocrinol* **52**. doi:10.1530/JME-13-0274

1035 Troutwine B, Gontarz P, Minowa R, Monstad-Rios A, Konjikusic M, Sepich DS, Kwon RY,
1036 Solnica-Krezel L, Gray RS. 2019. The Reissner Fiber is Highly Dynamic in Vivo and
1037 Controls Morphogenesis of the Spine. *SSRN Electron J* 1–10.
1038 doi:10.2139/ssrn.3486025

1039 Vaudry H, Leprince J, Chatenet D, Fournier A, Lambert DG, Le Mével JC, Ohlstein EH,
1040 Schwertani A, Tostivint H, Vaudry D. 2015. International union of basic and clinical
1041 pharmacology. XCII. Urotensin II, urotensin II–related peptide, and their receptor: From
1042 structure to function. *Pharmacol Rev* **67**:214–258. doi:10.1124/pr.114.009480

1043 Wang Z, Nishimura Y, Shimada Y, Umemoto N, Hirano M, Zang L, Oka T, Sakamoto C,
1044 Kuroyanagi J, Tanaka T. 2009. Zebrafish β-adrenergic receptor mRNA expression and
1045 control of pigmentation. *Gene* **446**:18–27. doi:10.1016/j.gene.2009.06.005

1046 Yang L, Rastegar S, Strähle U. 2010. Regulatory interactions specifying Kolmer-Agduhr
1047 interneurons. *Development* **137**:2713–2722. doi:10.1242/dev.048470

1048 Zhang X, Jia S, Chen Z, Chong YL, Xie H, Feng D, Wu X, Song DZ, Roy S, Zhao C. 2018.
1049 Cilia-driven cerebrospinal fluid flow directs expression of urotensin neuropeptides to
1050 straighten the vertebrate body axis. *Nat Genet* **50**:1666–1673. doi:10.1038/s41588-018-
1051 0260-3

1052

Supplementary Figures

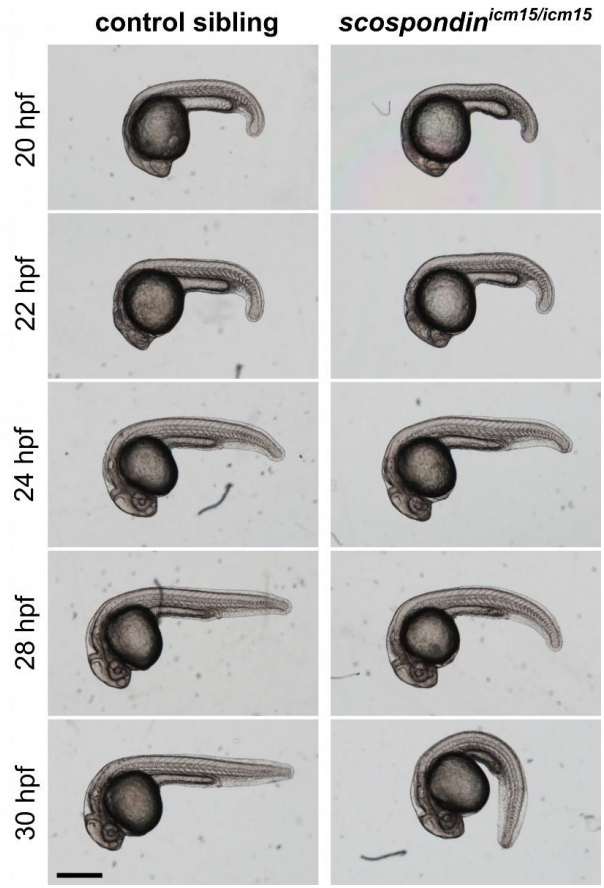

Figure 1 - Figure Supplement 1. Time course of the evolution of body axis geometry from 20 to 30 hpf in *scospondin*$^{icm15/icm15}$ mutants.

Representative images of the morphology of a control sibling (left) and a *scospondin*$^{icm15/icm15}$ embryo (right) followed over time at 20, 22, 24, 28 and 30 hpf. Embryos were obtained from a mating of *scospondin*$^{icm15/+}$ parents, staged at 20 hpf and maintained at 28.5°C. Body axis curvature in *scospondin*$^{icm15/icm15}$ mutants becomes visible as early as 28 hpf and fully recognizable at 30 hpf. Scale bar: 0.5 mm.

Figure 1 - source data 1. Data for figure 1B-C

Figure 1 - source data 2. Up- and down-regulated transcripts in curled-down *scospondin* mutants compared to their control siblings.

After filtering for low expression, we kept a list of genes that were differentially expressed in null *scospondin*$^{icm13/icm13}$ and hypomorphic *scospondin*$^{icm15/icm15}$ mutant embryos at 48 hpf. The table shows the average fold changes in the two alleles and their mean. Genes are ranked based on their p-value that compare the reproducibility of the change inside and between the two alleles using a GLM framework. We adjusted the false discovery rate due to multiple comparisons using the Benjamini-Hochberg procedure (see Material and Methods for details). The raw RNA-seq data have been deposited in the ArrayExpress database at EMBL-EBI (www.ebi.ac.uk/arrayexpress) under accession number E-MTAB-9615.

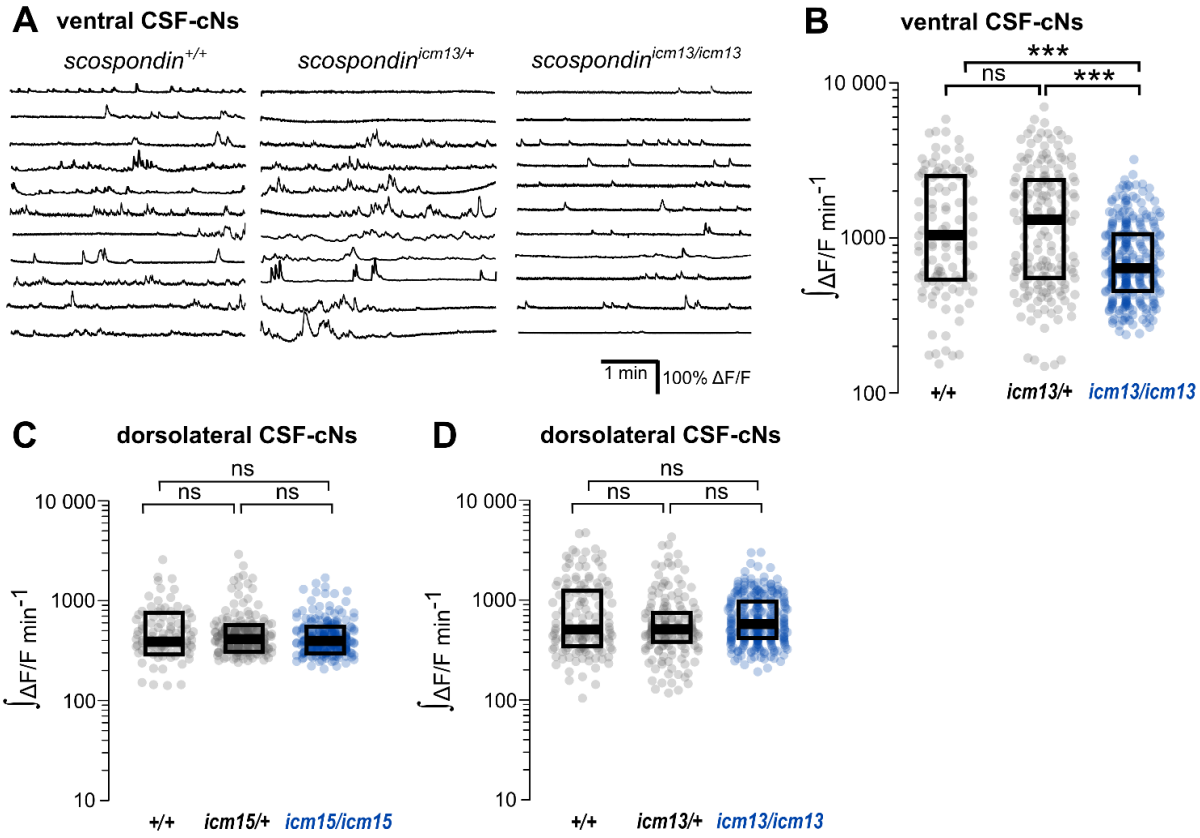

Figure 2 - Figure Supplement 1. The spontaneous activity of dorso-lateral CSF-contacting neurons does not require the Reissner fiber in the embryo.

(**A**) Traces of calcium variations in ventral CSF-contacting neurons at 30 hpf in wild type (*scospondin*$^{+/+}$), heterozygous (*scospondin*$^{icm13/+}$) and *scospondin*$^{icm13/icm13}$ null mutants. Sample traces from individual cells with integral ΔF/F values ranging around the median distribution of the imaged population are represented for each genotype (n=11). (**B**) Quantification of the normalized integrated calcium variation over time of ventral CSF-contacting neurons in wild type (+/+), heterozygous (*icm13*/+) and *scospondin*$^{icm13/icm13}$ mutants (*icm13/icm13*, blue). Data were collected from 3 independent experiments and include 8 wild type embryos (n=107 cells), 13 heterozygous embryos (n=176 cells) and 22 *scospondin*$^{icm15/icm15}$ mutants (n=277 cells). Each point represents a single cell. Bottom and top edges of the boxes indicate the 1st and 3rd quartiles. Bold lines represent the median value for each distribution. ns p>0.05, *** p<0.001 (Kolmogorov-Smirnov test). (**C**, **D**) Quantification of the normalized integrated calcium variations over time of dorsolateral CSF-contacting neurons in 30 hpf embryos obtained from *scospondin*$^{icm15/+}$ incrosses (**C**) and *scospondin*$^{icm13/+}$ incrosses (**D**) n=95, 243 and 255 cells in wild type, heterozygous and *scospondin*$^{icm15/icm15}$ embryos respectively (**C**); n=141, 176 and 168 cells in wild type, heterozygous and *scospondin*$^{icm13/icm13}$ embryos respectively (**D**). ns p>0.05 (Kolmogorov-Smirnov test).

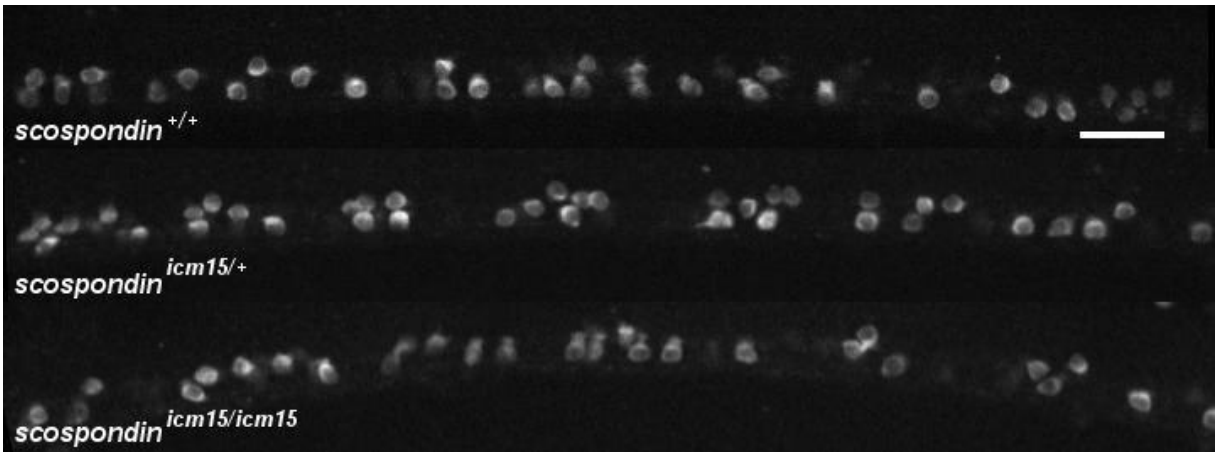

Figure 2- Video 1. Intracellular calcium transients of ventral CSF-contacting neurons are reduced in *scospondin* mutants.

Sagittal views of the spinal cord of *Tg(pkd2l1:GCaMP5G)* embryos at 30 hpf. *scospondin*$^{+/+}$ (top), *scospondin*$^{icm15/+}$ (middle) and *scospondin*$^{icm15/icm15}$ siblings (bottom) are represented. In wild type and heterozygous embryos, ventral CSF-contacting neurons are more active that dorso-lateral ones. Note the sharp decrease in calcium variations of ventral CSF contacting neurons in the homozygous mutant embryo compared to wild type and heterozygous counterparts. Data were collected at 4 Hz and displayed at 80 Hz. Scale bar: 30 µm.

Figure 2 - source data 1. Data for figure 2C and figure supplement 1B-C

A

control mRNA injection

	+/+	+/-	-/-
straight	3	8	0
curled up	0	0	0
curled down	0	0	12

B

control mRNA +*urp2* injection

	+/+	+/-	-/-
straight	20	43	**2**
curled up	1	3	**2**
curled down	0	0	9

Figure 3 -figure supplement 1. *urp2* overexpression recues body axis curvature defects in *scospondin* mutants.

Summary of straight, curled-up and curled-down phenotypes detected in wild type (+/+), *scospondin*$^{icm15/+}$ (+/-) and *scospondin*$^{icm15/icm15}$ mutant embryos (-/-) at 48 hpf after one cell stage injection of control mRNA (**A**) or control +*urp2* mRNA (**B**). Note that 2 mutant (-/-) embryos were detected as straight and 2 as curled-up upon *urp2* overexpression. Data were collected over 3 independent clutches.

Figure 3 - source data 1. Data for figure 3D

Figure 4 - source data 1. Data for figure 4C-E

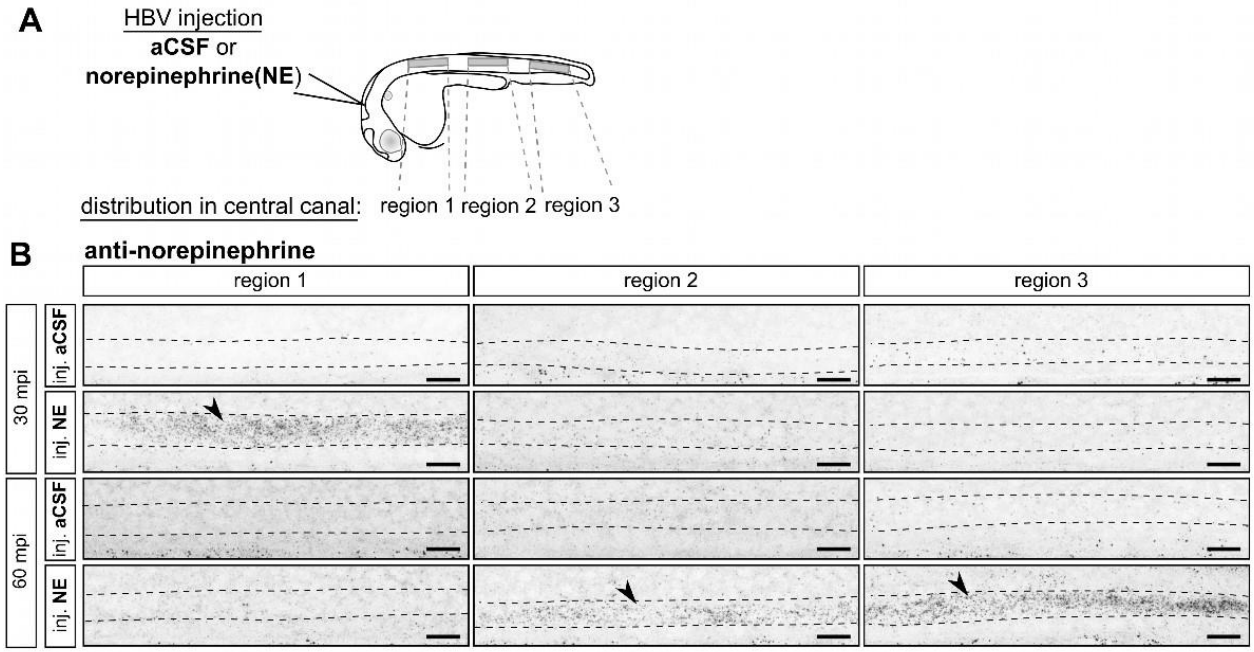

Figure 5-Figure Supplement 1. Exogenous norepinephrine injected in brain ventricles is transported to the spinal cord and saturates the central canal 60 minutes post-injection.

(**A**) 30 hpf embryos were mounted laterally and injected in the hindbrain ventricle (HBV) with either aCSF or 3mM norepinephrine (NE). Embryos from each group were fixed 30 and 60 minutes post-injection (mpi) and processed for an immunostaining against norepinephrine. Three regions in the spinal cord were imaged for each experimental condition (boxed regions): above the yolk (rostral, region 1), above the yolk extension (middle, region 2) and after the anal region (caudal, region 3). (**B**) Representative maximal z-projections of norepinephrine-positive signals detected after either the injection of aCSF (inj. aCSF) or exogenous norepinephrine (inj. NE), 30 and 60 minutes post-injection (mpi). The same imaging parameters and image processing parameters were applied to all experimental groups to avoid saturation for the most intense signals. Sagittal views of the three regions of the spinal cord shown in (**A**) are represented for a single representative embryo (n=7 embryos 30 minutes post-aCSF injection; n=7 embryos 30 minutes post-norepinephrine injection; n=6 embryos 60 minutes post-aCSF injection; n=8 embryos 60 minutes post-norepinephrine injection). Note that norepinephrine injected in the HBV saturates the central canal of the spinal cord (delineated by dotted lines) in the rostral most region 30 minutes post-injection, and the caudal most region 60 minutes post-injection (arrowheads). Embryos are oriented dorsal to the top and rostral to the left. Scale bars: 10 µm.

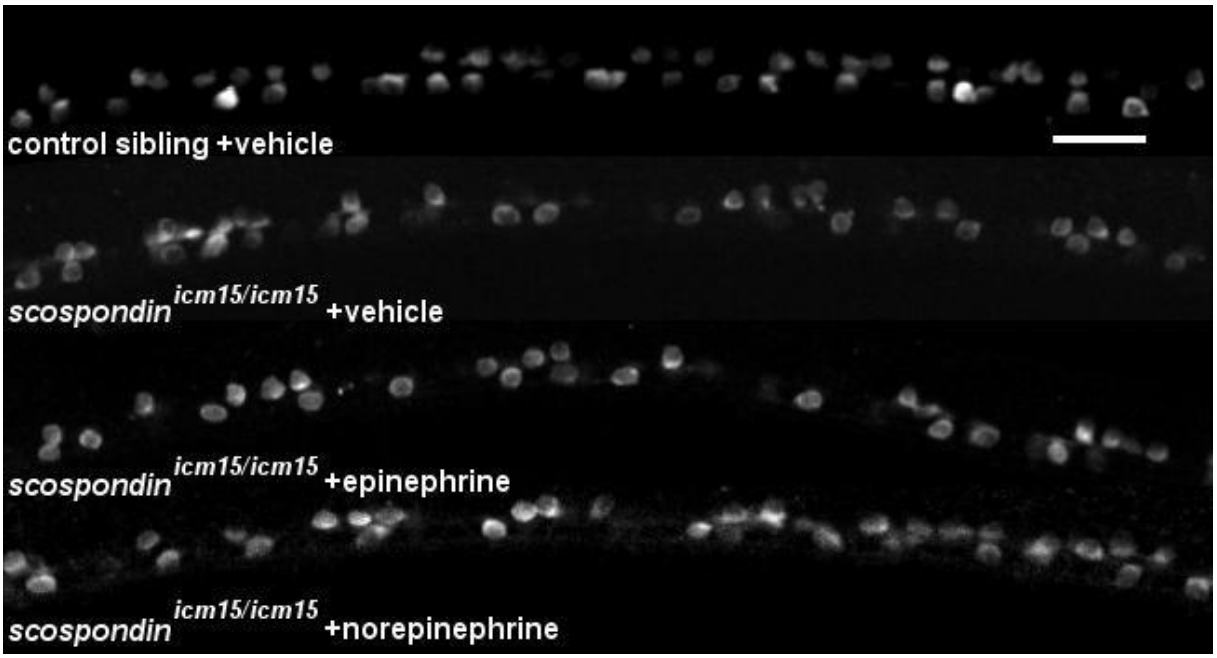

Figure 5- Video 1. Epinephrine and norepinephrine restore intracellular calcium transients of ventral CSF-contacting neurons in *scospondin* mutants.

Sagittal views of the spinal cord of *Tg(pkd2l1:GCaMP5G)* embryos at 30 hpf in a straight control sibling (top) and curled-down *scospondin*$^{icm15/icm15}$ mutants after vehicle, epinephrine or norepinephrine injections in the hindbrain ventricle. Note that calcium transients are restored in a subset of ventral CSF-contacting neurons of *scospondin*$^{icm15/icm15}$ embryos that received epinephrine and norepinephrine injections compared to mutants that received a vehicle injection. Data were collected at 4 Hz and displayed at 80 Hz. Scale bar: 30 µm.

Figure 5 - source data 1. Data for figure 5D-E

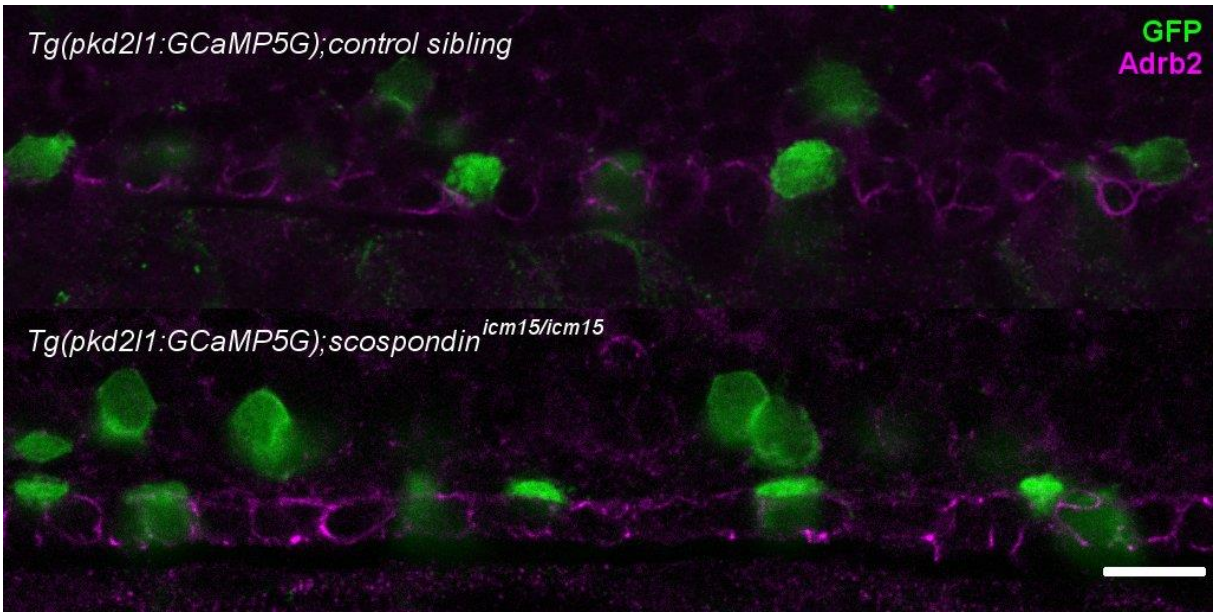

Figure 6 - Video 1. Adrb2 is expressed in the midline of the ventral most region of the neural tube that is different from that of CSF-contacting neurons.

Z-stack of a *Tg(pkd2l1:GCaMP5G)* control sibling (top) and a *Tg(pkd2l1:GCaMP5G); scospondin*$^{icm15/icm15}$ mutant (bottom) at 30 hpf immunostained against GFP (green) and Adrb2 (magenta). In both cases, Adrb2-postive domains are inserted between two rows of GFP-positive ventral CSF-contacting neurons (both domains are not colocalized). The video represents a 20.5 µm deep slice (0.5 µm z-step) for both embryos. Scale bar: 10 µm.